This is the author's accepted manuscript of:

Ming C, Breef-Pilz A, Howard D, Schreiber M. 2024. Geochemical drivers of manganese removal in drinking water reservoirs under hypolimnetic oxygenation. Applied Geochemistry 172: 106120. https://doi.org/10.1016/j.apgeochem.2024.106120

Revised manuscript with no changes marked
Click here to view linked References

Geochemical drivers of manganese removal in drinking water reservoirs under hypolimnetic oxygenation

Cissy L. Ming
Affiliation: Department of Geosciences, Virginia Tech
Email: cissy.ming@yahoo.com
ORCID ID: 0000-0003-0316-2315

Adrienne Breef-Pilz
Affiliation: Department of Biological Sciences, Virginia Tech
Email: abreefpilz@vt.edu
ORCID ID: 0000-0002-6759-0063

Dexter W. Howard
Affiliation: Department of Biological Sciences, Virginia Tech
Email: dwh1998@vt.edu
ORCID ID: 0000-0002-6118-2149

Madeline E. Schreiber (corresponding author)
Affiliation: Department of Geosciences, Virginia Tech
Email: mschreib@vt.edu
ORCID ID: 0000-0002-1858-7730

Keywords: metals, in situ treatment, Falling Creek Reservoir, Carvins Cove Reservoir, oxidation, water quality, southwest Virginia

Author attribution: CLM and MES developed the original project ideas. CLM and MES planned batch experiments. CLM conducted the batch experiments. ABP and DWH collected field samples and processed data. CLM and MES wrote the manuscript, based on the thesis of CLM. All authors edited and revised the manuscript.

Abstract: Manganese (Mn) is a naturally occurring contaminant commonly found in drinking water supplies. In lakes and reservoirs, water authorities increasingly use *in situ* treatment by hypolimnetic oxygenation (HOx) systems to remove metals such as Mn from the water column. HOx systems introduce dissolved oxygen (DO) to the bottom waters (hypolimnion) to promote oxidation and subsequent removal of metals from the water column. Previous laboratory studies have shown the importance of individual geochemical drivers (pH, alkalinity, mineral surfaces) on Mn oxidation, but few studies have examined the influence of these drivers of Mn removal in concert. In this study, we conducted field monitoring and laboratory experiments to examine how pH, alkalinity and the presence of mineral particles influence Mn removal at two drinking water reservoirs in southwest Virginia, both with HOx systems: Falling Creek Reservoir (FCR) and Carvins Cove Reservoir (CCR). Both reservoirs have had historical issues with elevated (> 0.05 mg/L) Mn concentrations during seasonal stratification (May-October). Watershed geology contributes to differences in pH and alkalinity between the reservoirs, with FCR having lower historical medians of hypolimnetic pH and alkalinity (6.6 and 18 mg/L $CaCO_3$, respectively) than CCR (7.2 and 62 mg/L $CaCO_3$, respectively).

Results of laboratory experiments examining the influence of pH on Mn removal showed substantial Mn loss within 14 days only under high pH (10) conditions. Mn removal did not occur at pH 6 or 8 over the same 14-day period. In experiments with pH 10 and alkalinity > 70 mg/L $CaCO_3$, near-total Mn removal occurred within 2 hours. Mn removal occurred concurrently with precipitation of microscopic (<5 μm) particles, followed by formation of macroscopic (>100 μm) particles. Particles of both size classes were identified as Mn oxides (MnOx). These observations suggest that increasing pH and alkalinity promotes Mn oxidation and subsequent removal from solution. Results of experiments with pH 10 and alkalinity > 70 mg/L $CaCO_3$ suggest that heterogeneous oxidation by MnOx partially drives rapid Mn removal. Thus, initial formation of MnOx creates a positive feedback loop that can enhance additional Mn loss. In experiments using water collected from FCR and CCR, we observed rapid Mn removal in unfiltered water (0.002 to 0.05 d^{-1}) but no significant removal of Mn in filtered water. These results, in combination with results of analysis of particles collected from reservoir water, suggest that minerals present in the water column likely catalyze MnOx formation. Together, our experimental results suggest that heterogenous oxidation is an important process of Mn removal, while pH and alkalinity variations of the range expected in natural freshwaters contribute less to differential Mn removal. The formation of MnOx particles during *in situ* oxygenation, as well as the presence of suspended minerals that occur naturally in water columns, play an important role in promoting Mn oxidation and should be accounted for in Mn removal treatment strategies.

1 Introduction

The presence of manganese (Mn) in freshwater systems degrades water quality in many locations worldwide (World Health Organization, 2021). The U.S. Environmental Protection Agency (U.S. EPA) has a secondary maximum contaminant level (SMCL) of 0.05 mg/L for Mn, which is a non-legally enforceable standard to address aesthetic issues, such as taste, odor and staining. The U.S. EPA does not currently regulate Mn concentrations in drinking water for public health protection. However, in 2021, the World Health Organization released a provisional health guideline of 0.08 mg/L for Mn in drinking water due to concerns about childhood neurological deficits linked to Mn exposure (Bouchard et al., 2011; Oulhote et al., 2014; Wasserman et al., 2011), indicating that Mn is a public health issue in addition to an aesthetic one. Manganese is prevalent in freshwater systems that provide drinking water for populations (Eaton, 2021). For example, Belitz et al. (2022) estimated that more than 10 million people in the U.S. may be impacted by high concentrations of Mn in groundwater used for drinking water.

Manganese can enter freshwater through weathering of Mn-rich soils (Gillispie et al., 2016) and bedrock (De Vitre and Davison, 1993). The solubility of Mn phases is strongly controlled by oxidation-reduction reactions, which alter the oxidation states of Mn. In freshwater, three oxidation states of Mn – Mn(II), Mn(III) and Mn(IV) – are stable, each with different solubilities (Davison, 1993). Mn(II) is the soluble form of Mn, which is predominantly found under reducing conditions. Under oxidizing conditions, Mn is favored to exist as Mn(III) or Mn(IV), which typically form less soluble solids. Although oxygen-rich waters favor the oxidation of Mn(II) to Mn(III) and Mn(IV), Mn(II) persists in surface waters due to the slow rate of Mn oxidation under typical pH (6-8) of freshwaters (Davison, 1993).

In temperate lakes and reservoirs, seasonal processes influence the oxidation-reduction reactions that drive Mn cycling. During summer months, non-uniform warming creates a density contrast between the epilimnion (surface waters) and hypolimnion (deep waters), causing water column stratification. During stratification, microbial consumption of oxygen in bottom sediment and the hypolimnion can result in anoxic conditions, creating favorable conditions for microbial reduction of Mn(IV) and subsequent upward diffusion of Mn(II), resulting in accumulation of soluble Mn(II) in the hypolimnion (Krueger et al., 2020). As temperatures cool in fall, the decreasing density contrast between the epilimnion and hypolimnion weakens stratification, until

the hypolimnion and epilimnion mix (turnover). Turnover introduces oxygen-rich water from the surface to the whole water column, creating conditions favorable for the oxidation of Mn(II) into insoluble Mn oxides (MnOx) that settle to the bottom sediments (Bryant et al., 2011; Davison, 1993; Hamilton-Taylor et al., 1996; Krueger et al., 2020; Scholtysik et al., 2020).

Although Mn cycling at the lake and reservoir scale has been well-studied (Chapnick et al., 1982; De Vitre and Davison, 1993; Wetzel, 2001) and several recent models of Mn cycling in reservoirs have been published (Zhang et al., 2021; Zhang et al., 2024), the impacts of lake and reservoir geochemistry on mechanisms and rates of Mn removal remain unresolved. Laboratory studies show that processes such as oxidation, non-redox precipitation of Mn minerals, adsorption and mineral-catalyzed (heterogeneous) oxidation strongly influence Mn removal (**Table 1**). The rate of Mn oxidation is highly pH-dependent; increasing pH by one unit above 7 results in a two orders of magnitude decrease in Mn(II) half-life (Davison, 1993). The presence of Mn-oxidizing bacteria accelerates Mn oxidation, allowing a normally monthslong reaction to proceed within days to weeks (Chapnick et al., 1982; Diem and Stumm, 1984; Friedl et al., 1997; Godwin et al., 2020; Tebo et al., 2005).

Aqueous carbonate concentrations, which contribute to alkalinity of freshwaters, may also influence Mn solubility in freshwater bodies. Carbonates in freshwater can promote precipitation of Mn carbonates and influence oxidation rate by affecting water column pH. Increased carbonate concentrations in freshwater can promote precipitation of Mn as Mn-rich calcite or rhodochrosite ($MnCO_3$) in bottom sediment (Davison, 1993; Herndon et al., 2018; Scholtysik et al., 2020; Thibault de Chanvalon et al., 2023; Wittkop et al., 2020). Formation of Mn-containing carbonates can facilitate further Mn removal as rhodochrosite precipitates around the “seed” crystal. In addition, increased alkalinity can maintain alkaline pH for prolonged periods, keeping water in conditions favorable for rapid Mn oxidation (Hem, 1963).

Surfaces of particulate minerals suspended in the water column can also accelerate Mn removal from water by adsorbing Mn(II) and catalyzing Mn oxidation (heterogeneous oxidation). Low-oxidation state transition metals such as Mn(II) adsorb onto mineral particles, including MnO_2, and settle with the particles, a process that becomes more favorable at pH>7.5 for MnO_2 (Neculita and Rosa, 2019; Tipping et al., 1984). In addition to adsorption, Mn(II) oxidation can be catalyzed by reactive mineral surfaces, including rhodochrosite (Diem and Stumm, 1984), iron (Fe) oxides and hydroxides (Davies and Morgan, 1989; Junta and Hochella

Jr, 1994; Lan et al., 2017; Madden and Hochella Jr, 2005), clays (Wilson, 1980; Yang et al., 2023) and Mn oxides and hydroxides (Elzinga, 2011; Hsiung and Tisue, 1994; Lefkowitz et al., 2013; Post, 1999; Zhu et al., 2020). Work by Morgan (2005) shows that in air-saturated solutions at pH 8, the half-life of Mn(II) oxidation decreases from 288 days to 29 days when the reaction is catalyzed by a solid surface.

These complex geochemical processes controlling Mn cycling in freshwaters present an ongoing challenge for drinking water treatment. Water treatment plants use physical (separation clarification, filtration), chemical (ion exchange, sorption, oxidation) and/or biological (oxidation) processes to remove Mn. These treatments can be expensive and create waste products that require proper disposal (Kohl and Medlar, 2006; Tobiason et al., 2016). In the past several decades, *in situ* treatments such as hypolimnetic oxygenation (HOx) have been increasingly utilized in drinking water supplies for removal of metals, including Mn (Preece et al., 2019; Semasinghe and Rousso, 2023). Without disrupting stratification, HOx systems introduce oxygen in the hypolimnion to accomplish three goals: 1) to promote oxic conditions in the hypolimnion and encourage oxidation and removal of reduced metals (such as Mn); 2) to promote oxic conditions in the upper sediment and prevent metal reduction by deepening the redox interface in sediment; and 3) to prevent upward diffusion of reduced metals from sediment into the water column (Li et al., 2019; Preece et al., 2019).

Case studies of HOx systems in lakes and reservoirs have found mixed results on soluble Mn removal (Semasinghe and Rousso, 2023). For example, Dent et al. (2014) observed substantial declines in soluble Mn after eight hours of oxygenation in North Twin Lake (Washington, USA). However, 94% of removed Mn was re-mobilized within one week. In Lake Pleasant (Minnesota, USA), HOx activation improved Mn removal but Mn concentrations in the hypolimnion still remained elevated, with a median of 0.45 mg/L (Austin et al., 2019). In southwest Virginia, the Western Virginia Water Authority (WVWA) installed HOx systems in Carvins Cove Reservoir (CCR) in 2005 (Gantzer et al., 2009b) and Falling Creek Reservoir (FCR) in 2012 (Gerling et al., 2014) to address several water quality issues. With year-round operation in CCR, HOx has lowered soluble Mn in the bulk hypolimnion to < 0.05 mg/L (Bryant et al., 2011; Gantzer et al., 2009a) but high Mn concentrations (up to 5 mg/L) have been measured near the sediment-water interface, which is below the depth of oxygen introduction. In FCR, HOx operation is typically April-October but there have been periods of inactivation since

installation. When the HOx is activated, Mn concentrations in the hypolimnion are below 2 mg/L, but during periods of deactivation, Mn can reach 4 mg/L (Schreiber et al., 2023).

Previous work by Munger et al. (2016) suggested that geochemical differences in drinking water reservoirs may impact Mn removal outcomes. For example, differences in bedrock geology (i.e., carbonate bedrock vs. crystalline bedrock) can influence pH and alkalinity of surface- and groundwater through water-rock reactions. Dissolution of carbonate bedrock introduces soluble carbonate species to water bodies, which contributes to higher alkalinity and pH buffering capacity of the water. The addition of soluble carbonate species also create favorable conditions for precipitation of Mn carbonates by shifting the water column chemistry toward saturation. In addition minerals commonly found in freshwater, such as Mn and Fe hydroxides as well as clays, can adsorb Mn and catalyze Mn oxidation in solution. Thus, multiple geochemical processes operating within reservoirs can affect Mn removal rate, but few studies examine their impacts in concert.

In this study, we conducted laboratory experiments combined with field monitoring to examine geochemical drivers of Mn removal rates in FCR and CCR, two drinking water reservoirs in southwest Virginia with different hypolimnetic pH and alkalinity due to variations in watershed geology. To address our objective, we conducted laboratory experiments using both synthetic solutions and reservoir water. We monitored solution chemistry and characterized particles that formed in the experiments. In addition, we conducted field monitoring in the two reservoirs to contextualize the experimental results. Through examining the factors that influence Mn removal in these reservoirs, our study offers broader insights on the key geochemical drivers that play a role in removing Mn in drinking water reservoirs.

2 Methods

2.1 Site Description

Falling Creek Reservoir (FCR; **Figure 1**) in Vinton, VA, USA serves as a reserve water supply for Roanoke, VA. FCR is a eutrophic reservoir with a maximum depth of 9.3 m and surface area of 0.119 km^2 (Krueger et al., 2020). Land cover within the watershed of FCR is over 90% deciduous and mixed forest (Stroud Research Center, 2017). FCR is located in the Blue Ridge Province of Virginia, with a watershed almost entirely underlain by varieties of granulite and granitic gneisses (**Figure S1**) (Woodward, 1932). Water inflows to FCR primarily through a

stream connected to nearby Beaverdam Reservoir. A secondary inflow is located within a wetland at the reservoir's northern shore. An outlet stream maintains stable water levels by draining excess inflow. During stratification, the upper boundary of FCR's hypolimnion exhibits a median depth of 3.8 m (Krueger et al., 2020).

The WVWA installed a side stream super-saturation HOx system in fall 2012. This system withdraws hypolimnetic water, supersaturates it with dissolved oxygen (DO), then returns the supersaturated water to mix with the hypolimnion (Gerling et al., 2014; **Table 2**). Since 2013, the HOx system in FCR has been periodically activated and deactivated for whole-reservoir ecological experiments or maintenance (Carey et al., 2022). In 2022, the HOx was turned on in mid-May and remained operational until mid-December, with a few days-long interruptions in operation due to maintenance.

Carvins Cove Reservoir (CCR; **Figure 1**) in Roanoke, VA, USA is a main water source for the city of Roanoke, VA. CCR is a eutrophic reservoir with a maximum depth of 23 m and a surface area of 2.5 km^2 (Gantzer et al., 2009b; Man et al., 2020). Also located in the Blue Ridge, the watershed of CCR is 92% forested, but includes less than 1% residential and agricultural land cover (Stroud Research Center, 2017). CCR has five primary inflows: Sawmill Branch, Tinker Creek, Catawba Creek, Horsepen Branch and Carvin Creek (Roland, 1970). The watersheds of three out of five of these inflows are underlain by shale and sandstone, while Tinker Creek drains a watershed containing carbonate formations (Moosdorf et al., 2010; Roland, 1970; **Figure S1**). Flow from Catawba Creek and Tinker Creek only enters CCR when the WVWA diverts discharge from either stream into CCR during periods of low water level. Roland (1970) found that introducing Tinker Creek water into CCR raised the reservoir's water column pH and alkalinity, which indicates that periodic introduction of water from that inflow may be associated with historical variations in alkalinity. During stratification, the upper boundary of the hypolimnion typically falls at 5-6 meters depth (Gantzer et al., 2009b; Man et al., 2020).

The WVWA installed and activated a line diffuser HOx system in August 2005 (**Table 2**). HOx operation typically continues year-round in CCR, though the volume of oxygen introduced by the system is decreased after turnover.

Historical water quality data in the reservoirs show that pH is lower in the hypolimnion of FCR than CCR, with median hypolimnetic pH values of 6.6 in FCR and 7.2 in CCR (Bryant et al., 2011; Carey et al., 2024). Historical data also show lower hypolimnetic alkalinity in FCR

(median 18 mg/L $CaCO_3$) compared to CCR (median 62 mg/L $CaCO_3$) (Western Virginia Water Authority, n.d.)

2.2 Reservoir Sampling

At FCR, sampling of the reservoir water column occurred weekly from mid-March to November 2022. For the remainder of the year, we sampled monthly. At the deepest point of FCR (site 50), we collected samples for metals, and for anions during weeks when CCR was sampled. Both metals and anions were sampled at the surface (0.1 m), 1.6 m, 3.8 m, 5.0 m, 6.2 m, 8.0 m and 9.0 m using a 4 L Van Dorn sampler (Wildlife Supply Company; Yulee, FL). Metals samples were also collected close to the weir on FCR's intake (site 100) and at the wetland inflow (site 200) (see **Figure 1; Table S1**). At each sampled depth, ~14 mL of unfiltered water was poured from the Van Dorn into a triple-rinsed 15 mL centrifuge tube for total metals analysis. For soluble metals, ~14 mL of water from the sampler was syringe filtered (0.45 μm nylon) into a triple-rinsed 15 mL centrifuge tube. Samples collected for metals were acidified with trace metals-grade nitric acid (HNO_3) to pH ≤2. For anion analysis, ~50 mL of water was syringe filtered (0.45 μm nylon) into a triple-rinsed 250 mL sample bottle; samples were frozen until analysis.

At site 50, alkalinity samples were collected in summer 2022 during weeks when CCR was sampled, at 0.1 m and 9.0 m. At 0.1 m, the sample was collected by immersing a 250 mL sample bottle in reservoir water and capping the bottle while underwater to minimize trapped atmospheric gasses. For samples collected at the deeper interval, water collected with a 4 L Van Dorn was poured into a plastic bucket, then the sample was collected as described for 0.1 m. Alkalinity samples were kept chilled until titration within 48 hours of collection.

At CCR, sampling occurred fortnightly from June to mid-August 2022. From August to November 2022, sampling frequency declined to monthly. At the deepest point of CCR (site 50), metals and anion samples were collected on each sample day at the surface (0.1 m), 1.5 m, 6.0 m, 9.0 m, 15.0 m and 20.0 m. Alkalinity samples were collected at 0.1 m and 20.0 m. Sample collection procedures were identical to FCR procedures. On dates when flow was observed in any tributaries, metal and anion samples were collected at the surface of the channel. Tributaries monitored and sampled for water were Sawmill Branch (site 301), Catawba Creek Tunnel (site 501), Tinker Creek Tunnel (site 400) and Carvins Creek Stream (site 201) (see **Figure 1; Table S1**).

At site 50 of both reservoirs, we measured temperature, DO, turbidity and pH profiles using a Seabird Electronics SBE19 plus high-resolution conductivity, temperature and depth meter (CTD). The CTD continuously recorded these parameters from the water surface to the base of the water column.

In July 2022, sediments were collected from the top meter of the CCR sediment column at site 50 using an Ekman Dredge. Powder X-ray diffraction (XRD) was conducted on the dried sediments using a Rigaku Miniflex II with a copper X-ray tube (Rigaku Corporation, Tokyo, Japan). The XRD spectrum was analyzed for mineral content using Match! Software, which matched peaks detected in the sediment sample to peaks found in reference minerals (Putz, n.d.).

2.3 Laboratory Experiments

We conducted two sets of experiments to examine the effects of pH and alkalinity on Mn removal rate. The first set, conducted in synthetic solutions, was designed to evaluate the kinetics and mechanisms of Mn removal under varying pH and alkalinity conditions. The second set of experiments was conducted in water collected from FCR and CCR to compare Mn removal rates between reservoirs and determine the impact of particulate matter on those rates.

2.3.1 pH and Alkalinity Experiments

We conducted laboratory experiments in air-saturated synthetic solutions to measure the effects of pH and alkalinity on Mn removal rate. We first examined Mn removal under eight treatments of varying pH and alkalinity over a 14-day period (**Table 3**). Samples were collected at 0, 1, 4, 7, 10 and 14 days. As considerable Mn removal was observed before 1 day, we did a separate experiment over 24 hours for conditions in which rapid removal was observed in the 14-day experiments. We collected samples at 0, 1, 2, 6, 12 and 24 hours.

The experiments were conducted in 500 mL acid-washed borosilicate flasks containing 250 mL of 1 mg/L $MnCl_2$ solution adjusted to varying alkalinity and pH (**Table 3, 4).** Where necessary for each treatment, we adjusted alkalinity of 1 mg/L $MnCl_2$ solutions by adding $NaHCO_3$, then raised pH by adding small aliquots of 0.1 N NaOH until attaining target pH within 0.5 units.. In initial solutions for each treatment, alkalinity was titrated (see section 2.4 for titration method); pH was measured using an OHaus benchtop pH meter, which was also used for all subsequent pH monitoring. Flasks were loosely covered with aluminum foil to block solution exposure to light and incubated at room temperature (20-25 ºC) on orbital shakers (150 rotations per minute, rpm) to maintain air-saturated DO conditions.

At each sampling interval, ~1.5 mL was withdrawn from each flask for pH measurement. We collected and syringe-filtered (0.22 μm nylon) 10 mL of solution from each flask into a 15 mL centrifuge tube for Mn analysis; these samples were acidified with trace metals-grade HNO_3. At the end of the experiments, 100 mL of solution from each treatment was titrated for alkalinity (see section 2.4 for titration method).

2.3.2 Reservoir Water Laboratory Experiments

We conducted an experiment using hypolimnetic water from FCR and CCR to compare Mn removal rates between reservoirs with and without particles. Our 10-day experiment tested Mn removal rates in unfiltered and filtered (0.45 μm) water from both reservoirs. Water was collected in mid-March 2023 (prior to stratification) at 9 m in FCR and 18 m in CCR using a Van Dorn sampler. At the time of water collection, DO concentrations were 12 mg/L (FCR) and 11.7 mg/L (CCR) and Mn concentrations within the hypolimnion of both reservoirs were below detection. We immediately transferred water into opaque brown plastic bottles and stored them under chilled conditions (1-3 °C). At the start of the experiment, we spiked FCR and CCR reservoir water with 100 mg/L $MnCl_2$ solution to achieve an initial Mn concentration of 1 mg/L. Our control consisted of 1 mg/L $MnCl_2$ in deionized (DI) water. Water used in filtered experiments was vacuum filtered (0.45μm) into flasks immediately before the experiment began.

Experiments containing 250 mL of reservoir water under filtered and unfiltered conditions were conducted in triplicate in acid-washed borosilicate flasks. Flasks were loosely covered in aluminum foil and incubated at room temperature on orbital shakers (150 rpm) to maintain air-saturated DO conditions. Sampling occurred at 0, 1, 4, 7 and 10 days. The procedures for sampling were the same as those described for 14-day and 24-hour experiments.

2.4 Water Analysis Methods

Samples from the laboratory experiments and reservoir monitoring were analyzed for a suite of metals, including Mn, by Inductively Coupled Plasma-Mass Spectrometry (ICP-MS; Thermo Electron iCAP RQ); the method detection limit for Mn was 0.001 mg/L. Samples for Mn analysis only for the 14-day experiment was conducted by ICP-AES, which had an method detection limit for Mn of 0.1 mg/L. Anion samples were analyzed for NO_3^-, Cl^- and SO_4^{-2} by ion chromatography (Metrohm 930 Compact IC Flex). The method's lower detection limit was 0.1 mg/L for the anions of interest.

For alkalinity titrations, 100 mL of sample was warmed to room temperature and transferred to a 150 mL flask. The sample was continually mixed at slow speed with a magnetic stir bar while drops of H_2SO_4 (0.16 M or 1.6 M, depending on the alkalinity) were added from a Hach digital titrator. We monitored pH changes with each addition of acid to calculate alkalinity. Alkalinity in mg/L $CaCO_3$ was calculated based on the number of H_2SO_4 drops added to reach endpoints of pH 4.5 and 4.2, which represent the depletion of CO_3^{-2} and HCO_3^-, respectively.

2.5 Particle Analysis Methods

We analyzed selected macroscopic (>100 μm) particles from synthetic solution and reservoir water experiments using a Field Emission Electron Probe Micro-analyzer (EPMA; JEOL, Tokyo, Japan) at the Virginia Tech Nanoscale Characterization and Fabrication Laboratory (NCFL). Visible particles were collected from experimental solutions and rinsed in nanopure water to remove salts. Particles were mounted on copper electrical tape by pipetting 10 μL of solution onto the tape, then allowing water to evaporate. Once desiccated, mounted samples were evaporation-coated with carbon (Heu et al., 2019). For each analyzed particle, we collected quantitative data on elemental compositions and qualitative element maps showing the relative abundances of elements on the particle surface. Identifying and determining the relative abundances of elements on the particle surface allowed us to identify the class of mineral formed, which informed our interpretation on the mechanisms of Mn removal. We also collected high-magnification scanning electron microscope (SEM) images of the particles' morphology and texture to further inform mineral identification.

We used Transmission Electron Microscopy (TEM; JEOL JEM 2100, Tokyo, Japan) at the Virginia Tech NCFL to characterize microscopic (<5 μm) particles in selected experiments. We used energy-dispersive X-ray spectroscopy (EDS) to determine elemental composition and selected area electron diffraction (SAED) to identify crystalline structure. The combination of EDS and SAED analyses informed our identification of possible mineral phases present. To collect microscopic particles for imaging and analysis, we collected 2 mL aliquots of visibly discolored experimental solution from selected experiments and preserved the aliquots at -18 °C before ultracentrifugation at 109000 relative centrifugal force (RCF) for 1 hour to concentrate particles (Learman et al., 2011). Prior to drop casting on a 300 mesh lacey carbon TEM grid, particles were resuspended in deionized water by sonication (Williams et al., 1996). For each

experiment, 2-3 grids were prepared with 10-20 μL of suspension transferred onto each grid by micropipette.

Diffraction patterns obtained from SAED were analyzed for d-spacing using the Gatan Digital Micrograph software package (Gatan Digital Micrograph, v. 3.5). Rings were manually identified and annotated on diffraction patterns. Based on d-spacings with a +/- 0.05 Å tolerance, diffraction pattern matches were identified in the American Mineralogist Crystal Structure Database among Mn oxide and hydroxide phases (Downs and Hall-Wallace, 2003).

2.6 Geochemical Calculations

Using the Spec8 module of Geochemist's Workbench (GWB), we ran speciation solubility calculations for the experimental solutions to support identification of minerals formed in our experiments (Bethke, 2022). We additionally used metals and anion concentrations obtained from the summer 2022 field campaign at FCR and CCR to determine favorability of precipitation for several Mn minerals in the reservoir water column.

2.7 Calculation of Mn Removal Rates

We used time series Mn concentration data from the laboratory experiments to calculate Mn removal rates. For the 24-hour high pH (10) and moderate alkalinity (70 mg/L $CaCO_3$) experiment, we calculated a second-order Mn(II) removal rate (mg/L^{-1} hr^{-1}). The second-order rate constant was calculated from the slope of a linear equation fit to the inverse of Mn concentration data averaged across triplicates vs. time (Rimstidt, 2014). We initially attempted to fit a linear equation to a first- and zero-order transformation of the Mn concentration data but found the best fit with a second-order transformation. For the FCR and CCR unfiltered experiments, we calculated the first-order Mn(II) removal rate (d^{-1}) by fitting a linear equation to the natural log of Mn concentration data averaged across triplicates (Rimstidt, 2014).

3 Results

3.1 Reservoir Water Quality Monitoring

Reservoir water quality time series data in 2022 for FCR (**Figure 2)** and CCR (**Figure 3**) are available in Carey et al. (2024) and Schreiber et al. (2023).

DO concentrations in the hypolimnion of FCR reached 11 mg/L prior to stratification in 2022 (**Figure 2**). However, from the onset of stratification in mid-May to turnover, DO

concentrations at and below the thermocline remained below 2 mg/L despite HOx operation. Following turnover in November, DO rose to above 4 mg/L and remained at or above 4 mg/L during the reminder of the year. Values of pH were circumneutral for most of the reservoir water column, with exception of pH close to 10 at the reservoir surface in June and July that coincided with an algal bloom observed in FCR (**Figure 2**). However, pH in the hypolimnion was steady during stratification, with a notable increase after turnover in November 2022.

Prior to stratification, Mn concentrations in FCR were < 0.1 mg/L (**Figure 2**). Starting in mid-May, Mn increased in the hypolimnion, concomitant with the decrease in DO concentration. By October, immediately preceding turnover, hypolimnetic Mn concentrations were generally ~ 1 mg/L but reached close to 3 mg/L at the sediment water interface (9 m). Total and soluble Mn concentrations in the hypolimnion were roughly equal (**Figure 2**), indicating that the majority of Mn in FCR is in dissolved, rather than particulate, form. Mn concentrations in the main inflows to FCR (sites 100 and 200) ranged from below detection to 0.11 mg/L (**Figure S2**). In contrast to the water column, soluble Mn from samples collected at the tributaries was often less than 50% of total Mn, indicating that much of the Mn entering FCR through the inflows is in particulate form. Concentrations of soluble and total Fe in the hypolimnion of FCR (**Figure S3**) reached 12 mg/L at the end of summer stratification, within a few weeks of turnover. Total Fe concentrations were significantly greater than soluble Fe, indicating that much of the Fe is in particulate form, consistent with the oxidation of Fe due to HOx.

Alkalinity concentrations measured in FCR samples collected in 2022 (**Table S2**) were consistent with historical values (median 18 mg/L) (**Figure 4**). Turbidity measured in the hypolimnion of FCR (9 m) from 2013-2022 was highly variable, ranging from 10 to over 80 NTUs (**Figure S4**). Concentrations of major cations (Ca, Mg, Na + K) and major anions (Cl and SO_4) were lower than 5 mg/L across depths and dates in FCR in 2022 (**Figure S5)** while nitrate concentrations were below the detection limit of 0.1 mg/L. Tributaries to FCR had cation concentrations similar to those observed in the reservoir, with Ca, Mg, and Na + K concentrations less than 5 mg/L (**Figure S6**).

In CCR, prior to onset of stratification in May 2022, DO concentrations in the hypolimnion were above 10 mg/L (**Figure 3**). In contrast to FCR, DO concentrations in CCR remained > 2 mg/L until July. However, despite the continuous HOx operation, a decline in DO concentrations to less than 2 mg/L in the hypolimnion began in late July and continued into fall.

DO concentration measured at 20 m reached a minimum of 0.18 mg/L in August 2022. Values of pH in the hypolimnion ranged between 7.1 and 8.6, with a mean of 7.45 (**Figure 3**). Higher pH (~8.5) was measured in the epilimnion in the late summer to early fall, likely due to algal blooms.

Mn concentrations in CCR were generally < 0.6 mg/L above 18 m (the depth of oxygen introduction) (**Figure 3**). However, at the sediment water interface (20-21 m), Mn concentrations increased starting in July, reaching close to 10 mg/L in late September, concomitant with low DO concentrations. In contrast to FCR, where Mn concentrations reached a maximum right before turnover, the Mn concentrations in CCR declined in October, more than a month before turnover, Similar to FCR, however, total and soluble Mn concentrations were roughly equal (**Figure 3**) indicating that the majority of Mn in CCR is in dissolved form. Total and soluble Mn concentrations in the tributaries to CCR (sites 201, 301, 400, 501) were less than 0.1 mg/L and were similar, suggesting that in contrast to FCR, Mn entering CCR through tributaries was mostly soluble (**Figure S2**). Concentrations of soluble and total Fe in the hypolimnion of CCR (**Figure S3**) were both close to the detection limit, indicating that the HOx system successfully suppresses Fe release from reservoir sediments into the water column.

Alkalinity concentrations measured in CCR in 2022 (**Table S2**) were lower than historical values (median 62 mg/L) (**Figure 4**). Turbidity measured in the hypolimnion of CCR from 2017-2022 was less variable than in FCR. Turbidity was less than 10 NTUs during the early summer and increased to around 20 NTUs during the late fall approaching turnover (**Figure S4**). Concentrations of Ca, Mg, Cl, and SO_4 were higher in CCR compared to FCR in 2022, with slightly lower concentrations for Na + K in CCR (**Figure S5).** Similar to FCR, nitrate concentrations were below detection (<0.1 mg/L). Tributaries to CCR had higher concentrations of Ca (up to 60 mg/L) and Mg (up to 20 mg/L) than FCR tributaries. Anion concentrations were highly variable, up to 8 mg/L for Cl and 25 mg/L for SO_4 (**Figure S6**).

3.1.2 Solubility Calculations

Based on solubility calculations using the GWB Spec8 module (**Table S3**), the hypolimnia of both reservoirs in summer 2022 were oversaturated with respect to birnessite and hausmannite and undersaturated with respect to rhodochrosite.

3.1.3 XRD of CCR sediments

XRD analyses of sediments collected from the surface sediment at CCR site 50 indicates presence of quartz and clay minerals similar to montmorillonite. The XRD analyses did not detect Fe or Mn phases in the sediment, but the lack of matches between the XRD spectra and Fe and Mn phase peaks does not preclude their presence (**Figure S7**).

3.2 pH and Alkalinity Laboratory Experiments

Laboratory experimental data are published in Ming and Schreiber (2023).

3.2.1 14-day experiments: Solution Chemistry

Over the 14-day pH and alkalinity experiments, we only observed decreases in soluble Mn concentration in solutions of high pH (10) (**Figure 5**). In high pH experiments with moderate (70 mg/L $CaCO_3$) or high (250 mg/L $CaCO_3$) alkalinity, the soluble Mn concentration declined to less than 20% of initial values within 24 hours. Declines in soluble Mn concentration occurred substantially faster in high pH/high alkalinity solutions compared to high pH/moderate alkalinity experiments, despite rapid losses of soluble Mn in both solutions. Slower declines of soluble Mn concentration were observed in high pH solutions with no alkalinity adjustment (**Figure 5B**).

During the experiment, we observed solution color changes and particle formation in experiments of high pH and moderate or high alkalinity. We observed a yellowish-brown color at 24-hours in experiments of high pH/moderate alkalinity, which persisted throughout. In the high pH/high alkalinity experiments, rusty brown to black aggregates formed within 24 hours (**Table S4**). In experiments of pH≤8, we observed no solution color changes or particle formation over the 14 days.

Alkalinity adjustment maintained consistent pH within high pH and moderate or high alkalinity solutions (**Figure 5**). Between 1 and 4 days, the pH in high pH solutions without alkalinity addition began to decline relative to pH of high pH solutions with added alkalinity; by day 14, the pH dropped over one unit from the initial pH.

Based on solubility calculations, Mn oxide precipitation was favored to occur over rhodochrosite precipitation in all high pH and moderate pH (~8) experiments. Based on the saturation index, a measure of a mineral's probability of precipitating, birnessite (δ-MnO_2) was most favored to precipitate by several orders of magnitude, with hausmannite also favored to precipitate. Rhodochrosite was undersaturated in high pH experiments but was at or slightly over saturation in moderate pH high alkalinity experiments. When pH remained constant in the Spec8

simulation, the calculated solubility of Mn minerals did not vary substantially with alkalinity (see **Table S5**).

3.2.2 24-hour experiments: Solution Chemistry

We observed significant decreases in soluble Mn concentrations within one hour in high pH solutions with moderate or high alkalinity (**Figure 6**). In contrast, we observed negligible changes in soluble Mn concentrations in control solutions, which lacked pH or alkalinity adjustment. In high pH/moderate alkalinity solutions, the vast majority of Mn removal occurred between 0-2 hours, with a minor drop in soluble Mn concentration at hour 6.

With sampling every few hours, we observed discoloration and particle formation in high pH and moderate or high alkalinity solutions within 12 hours. Upon initial experimental setup, these solutions displayed translucent yellow-brown coloration, which remained present for the experiment duration in high pH/moderate alkalinity solutions. Macroscopic rusty-brown particles formed between 6-12 hours. Between 6-12 hours, the high pH/high alkalinity solution became more opaque and a darker shade of brown (**Table S6**). Between 12-24 hours, the high pH/high alkalinity solution became clear while macroscopic particles remained, similar to visual observations at 1 day in the 14-day experiments.

3.3.1 24-hour experiment: Particle analysis

Macroscopic (>100 μm) particles sampled from high pH/moderate alkalinity and high pH/high alkalinity experiments at 24 hours contained abundant Mn and oxygen on their surfaces, as indicated by EDS element maps and quantitative analyses (**Figure 7**). We observed trace amounts of carbon on the particles likely introduced by carbon coating. Representative particles had pitted surface textures (**Figure 7**). Diameters of imaged particles ranged from 100-500 μm.

TEM-imaged microscopic (<5 μm) particles from high pH and moderate or high alkalinity solutions had similar morphologies, elemental compositions and crystal properties. The differences between the size ranges of TEM-imaged particles and macroscopic particles stem from the process used to isolate microscopic particles for TEM. In addition, the lacy carbon grids used for TEM were intended for particles at the lower end of the microscopic range. For both high pH/moderate alkalinity and high pH/high alkalinity solutions, particles were interlocking needle-like crystals aggregated in a dense mass (**Figure 8; Figure S8**). The aggregate particles were ~2 μm in diameter, and individual needles were nanosized (~10-20 nm in diameter). In the particle collected from the high pH/high alkalinity solution, we observed thin sheets on the

particle's periphery alongside the needles (**Figure S9**). EDS element maps indicate the particles from both experiments were composed of oxygen and Mn (**Figure 8**).

To identify the microscopic Mn minerals formed, we obtained d-spacings of the two particles from SAED analysis and calculated Mn mineral solubility for each experimental solution's composition using GWB. For the particle analyzed from the high pH/moderate alkalinity solution, d-spacings of the two major ring patterns were 2.24-2.49 Å and 1.51-1.52 Å (**Figure S10**). For the particle analyzed from the high pH/high alkalinity solution, d-spacings of the two major ring patterns were 2.28-2.46 Å and 1.39-1.44 Å **(Figure S10**). The combination of measured d-spacings, morphology, elemental composition and GWB calculations suggest birnessite and pyrolusite – both Mn(IV) minerals – as probable candidates for microscopic particles precipitated in the high pH/moderate alkalinity and high pH/high alkalinity solutions.

3.1.3 Reservoir water laboratory experiments: Solution Chemistry

We only observed significant Mn removal over 10 days in unfiltered reservoir water experiments (**Figure 9**). Significant Mn removal began within 24 hours in unfiltered FCR water, with near total Mn removal between 1-4 days. In unfiltered FCR water, soluble Mn concentrations continued to decline until day 7 at a first-order rate of 0.050 d^{-1}. Between days 7 and 10, Mn concentrations increased to approximately 50% of initial concentrations. In unfiltered CCR water, significant Mn removal was observed between day 4 and 10, with a first-order removal rate of 0.002 d^{-1}.

Initial visual observations of reservoir water from FCR and CCR were similar (**Table S7**). Water was clear but contained tan and black silt- to fine sand-sized particles. In unfiltered FCR water, translucent orange-pink discoloration and formation of rusty brown to black aggregates occurred between day 1 and 4 after Mn addition (**Figure 10, 11**). In unfiltered CCR water, both yellow-brown solution discoloration and formation of similar aggregate particles occurred between days 4 and 7 after Mn addition (**Figure 12**).

Observations in filtered reservoir water contrasted with those from unfiltered reservoir water. The filtered reservoir water and control solutions remained clear for the entire experiment; however, we observed scattered black silt-sized particles in FCR filtered experiments at 10 days. No visible particles formed in the CCR filtered experiments.

3.2.2 Reservoir water laboratory experiment: Particle Analysis

Morphologies and elemental compositions of visible particles collected from FCR and CCR unfiltered experiments were similar. In both, we observed macroscopic aggregates of platy and blocky particles (**Figures 10, 11**). The macroscopic aggregates were ~100 μm in diameter; platy and blocky particles within the aggregates were less than 10 μm in diameter. Element mapping with EPMA indicates that blocky and platy particles, which comprise the aggregates, contain abundant Si and O, which is consistent with their identification as silicate minerals (**Figure 10**).

The TEM-imaged microscopic particles from FCR unfiltered water were similar to one another in morphology, elemental composition and crystal properties. All imaged particles had crumpled sheet-like morphologies, with individual particles ~3-5 μm in diameter (**Figure 11**). EDS element maps indicate they are predominantly composed of Mn, Fe and O (**Figure 11**). Across the analyzed particles, d-spacings of the two major ring patterns were 2.21-2.58 Å and 1.38-1.53 Å. Based on the elemental composition, d-spacings and crumpled sheet morphology of particles, we suggest that the particles likely consist of aggregated birnessite.

4 Discussion

Below, we discuss drivers of Mn removal under HOx operation in lakes and reservoirs of different geochemical conditions. We hypothesize the mechanisms of rapid Mn removal observed in our high pH and moderate or high alkalinity experiments. We also address how the presence of particulates may impact Mn removal rates in the water columns of lakes and reservoirs. Finally, we describe implications of our study for drinking water treatment, discuss our study limitations and list outstanding questions raised by our results.

4.1 High pH and alkalinity can enhance Mn removal in freshwaters

Results of our laboratory experiments shed light on the independent impacts of pH and alkalinity on Mn removal rate, and how these drivers act together. Our experiments suggest that the combination of high pH (10) and moderate to high alkalinity (>70 mg/L) in freshwater can accelerate Mn removal. Considering the composition of our synthetic experimental solutions, the most probable mechanisms of Mn removal are: 1) oxidation of Mn(II) by DO to form Mn oxides; 2) reaction of Mn(II) with dissolved carbonate to form rhodochrosite; and 3) adsorption and/or heterogeneous (mineral-catalyzed) oxidation of Mn(II) by Mn oxides (**Figure 13**).

We propose Mn oxidation as the primary pathway of rapid Mn removal based on solution geochemistry, geochemical modeling and qualitative observations of particles. Both macroscopic and microscopic particles contained an abundance of Mn and oxygen and a lack of carbon, which is consistent with formation of Mn oxides. The lack of carbon detected within particles indicates that rhodochrosite precipitation did not occur in appreciable quantities. The morphology and color of macroscopic particles observed in our experiments matches those of Mn oxides formed in previously reported laboratory experiments addressing Mn oxidation (Hem, 1963; Learman et al., 2011; Tipping et al., 1984). Appearance of "brown turbidity" followed by macroscopic particle aggregation in high pH and moderate or high alkalinity solutions resembles the evolution documented by Learman et al. (2011). In experiments examining Mn oxide catalysis of Mn oxidation, Learman et al. (2011) identified Mn oxides or hydroxides in the microscopic particles discoloring the solution and in the macroscopic particles that subsequently formed. Hem and Lind (1983) and Hem (1963) reported on the greater favorability of Mn oxidation over rhodochrosite precipitation under basic (pH>7.5) and oxic conditions. Our results suggest that the main role of alkalinity in Mn removal in our experiments was to maintain the higher pH conditions that are favorable for faster Mn oxidation.

The near-total removal of soluble Mn within two hours in solutions of high pH (10) and moderate (70 mg/L) or high (250 mg/L) alkalinity suggests that Mn oxides adsorb Mn(II) or catalyze Mn oxidation. The catalysis of Mn oxidation by Mn oxides and hydroxides has a half-life of several hours, faster than Mn oxidation by DO under pH 10 conditions in the absence of catalysts (Cheng et al., 2020b; Learman et al., 2011). Our Mn concentration time series for the 24-hour experiments show the fastest Mn removal rates initially, before removal rates slow with the decrease in soluble Mn concentrations. This removal trend is consistent with expectations for mineral catalysis of Mn oxidation by Mn oxides, as removal is fastest when soluble Mn(II) is abundant but slows once less Mn(II) remains (Bethke, 2022).

Our data cannot conclusively determine whether Mn oxide particles drove further Mn removal via mineral catalysis, adsorption or both. Distinguishing between removal mechanisms has implications for freshwater Mn cycles, as adsorbed Mn remobilizes more readily than oxidized Mn (Hsiung and Tisue, 1994). Quantifying Mn removal by each mechanism is difficult without titration of particles for their average oxidation state or analysis by X-ray photoelectron spectroscopy (Hem, 1963). A low average oxidation state of particles would reflect dominance

of adsorption over oxidation because Mn(II) adsorption to Mn oxides does not involve Mn's transformation into a higher oxidation state. However, Mn oxidation transforms Mn(II) into Mn(III) or Mn(IV). Adsorption and Mn oxidation both grow more favorable under the high pH conditions in which we observed rapid Mn removal, which is supported by other studies (Lefkowitz et al., 2013). The point of zero charge for MnO_2 has been reported at values ranging from pH 2.4-6, meaning MnO_2 mineral surfaces are more negatively charged at high pH and therefore sorb Mn(II) more readily (Adams et al., 2009). In addition, Mn adsorption precedes Mn catalysis by Mn oxides, making the separate study of these removal mechanisms difficult (Lan et al., 2017).

4.2 Particulate matter can catalyze Mn oxidation and removal in freshwaters

In our reservoir water experiments, significant Mn removal was only observed in unfiltered water. Therefore, we propose that particles over 0.45 μm in diameter may be an important driver of Mn removal in FCR and CCR. The particles present in our experiments included minerals, organic matter and other suspended solids, all of which may drive Mn removal through separate pathways. Suspended particles in FCR may catalyze Mn oxidation and subsequent precipitation as Mn oxides. Possible mineral catalysts present in the water column include birnessite, a common Mn sheet mineral found at the oxic-anoxic boundary in lakes and reservoirs (Elzinga, 2016; Friedl et al., 1997). Within our unfiltered experiments, imaging and elemental analysis of macroscopic particles suggest that Mn oxides likely coat or nucleate on suspended particles. We interpret the aluminum and/or silicate-rich plates and blocks in our particles as primarily quartz and clay minerals based on XRD analysis of CCR sediment. Clay minerals – detected in surficial CCR sediments by this study – can catalyze Mn oxidation (Yang et al., 2023). The occurrence of Mn in close association with Al and Si in element maps of macroscopic particles is consistent with observations of preferential Mn oxide coating on quartzite and shale particles by Adams et al. (2009). At high magnification of Mn and oxygen-rich regions on the particles, the globular textures we observed are similar to Mn oxide textures reported in Adams et al. (2009) (probable birnessite) and Sánchez-España and Yusta (2019) (asbolane).

Our hypothesis of enhanced Mn removal by suspended particles is consistent with previous work that documented Mn oxidation's high sensitivity to mineral catalysis in freshwater (Godwin et al., 2020; Hsiung and Tisue, 1994). Godwin et al. (2020) proposed greater density of

suspended particles as one explanation for much greater Mn oxidation in the Western Basin of Lake Erie compared to the Eastern Basin. However, the results of our study do not address if and how the compositions of suspended particles in each reservoir may drive different Mn removal outcomes. Madden and Hochella Jr (2005) demonstrated that smaller particles have greater capacity to catalyze Mn oxidation, while other studies reported significantly different rates of Mn oxidation catalysis by minerals found in the natural environment (Lan et al., 2017; Learman et al., 2011).

In unfiltered reservoir experiments, we observed higher rates of Mn removal in FCR water relative to CCR water, a difference possibly due to initial suspended particle densities in the water we collected for our experiments. Using turbidity as a rough proxy for suspended particle density in the reservoir water column, our comparisons of 2013-2022 turbidity data from FCR and CCR shows marginally higher turbidity in FCR at the depths sampled for our experiments (**Figure S2**) (Carey et al., 2024). However, turbidity can be highly variable in FCR, and turbidity does not necessarily indicate the presence of minerals that facilitate Mn removal. Thus, it is currently unclear if the enhanced Mn removal in FCR vs. CCR is influenced by particle density.

4.3 Differences in alkalinity and pH between FCR and CCR don't influence Mn removal

We conducted laboratory experiments in reservoir water and synthetic solutions of modified pH and alkalinity to evaluate geochemical drivers of Mn removal in drinking water reservoirs. Based on historical data, we hypothesized that the combination of higher pH and alkalinity in CCR would enhance Mn removal in CCR relative to FCR. However, our field monitoring results do not support this hypothesis, partially because the differences in pH and alkalinity between the reservoirs were considerably smaller in 2022 than they were historically. The lack of inflow from the Tinker Creek Tunnel in summer 2022 may explain the lower pH and alkalinity in CCR compared with historic values. Tinker Creek Tunnel (site 400; see **Figure 1**) introduces higher pH and alkalinity water due to carbonates in its watershed, as documented by Roland (1970). Therefore, our data do not support our hypothesis that pH and alkalinity differences between FCR and CCR contribute substantially to differences in Mn removal rate.

4.4 Study limitations and suggestions for future work

We discuss several limitations of our work to contextualize interpretation of our results and to suggest improvements in future research. First, we used different pore size filtration

membranes to separate particulate Mn from soluble Mn in our field monitoring (0.45 μm) and our experimental monitoring (0.22 μm). Thus, soluble Mn concentrations observed during field monitoring and in our experiments are not directly comparable. The standard operating procedures for reservoir monitoring were established in 2014 and we continue to follow those procedures to allow for comparison of datasets over space and time (Schreiber et al., 2023). For the experiments, use of a smaller pore size filter was beneficial for evaluating Mn removal via formation of smaller-sized Mn oxides, which was described by Tobiason et al. (2016) in a water treatment context. Despite the smaller pore size used to define soluble Mn in our experiments, our TEM imaging of microscopic particles formed in experiments confirms the formation of Mn particles small enough to pass through a 0.22 μm filter.

In addition, the process of altering the pH and alkalinity in our synthetic solution experiments introduced concentrations of sodium (Na) and potassium (K) much higher than those found in natural waters, which may impact the reactions occurring in solution. The high concentrations of Na and K raise the ionic strength of our experimental solutions, increasing the probability of Mn precipitate aggregation (Hotze et al., 2010). The presence of Mn(II) and Na together in solution promote aggregation by neutralizing negative charges on MnOx surfaces and compressing the electric double-layer between particles (Cheng et al., 2020a). The concentration of Na in the high pH and moderate or high alkalinity solutions exceeds the minimum needed to destabilize MnOx enough to promote MnOx aggregation, based on the work of Cheng et al. (2020a). Therefore, high Na concentrations may have partially contributed to the formation of microscopic and macroscopic aggregates in the synthetic experiments. Our interpretation of reservoir water experiments and field data also does not address interactions between Mn and organic carbon that can influence Mn mineral stability (Li et al., 2021; Li et al., 2019).

Prior work by Munger et al. (2016) demonstrated that Mn-oxidizing microbes accelerate Mn oxidation in FCR. In addition, there is extensive evidence that microbes accelerate Mn oxidation by several orders of magnitude (Bargar et al., 2000; Cerrato et al., 2010; Tebo et al., 2005). We did not specifically compare the influence of microbial processes on Mn oxidation between FCR and CCR reservoirs, which limits the applicability of our results to other reservoirs. Future experiments could be designed to address these limitations to broaden our understanding of Mn removal mechanisms.

Last, the HOx systems operations differed between FCR and CCR, confounding comparisons between Mn removal rates and accumulation between the reservoirs. The HOx system in CCR operated at full capacity throughout the stratified period and continued at reduced capacity in winter. In contrast, the HOx in FCR was turned on in mid-May 2022 and was operational until mid-December, with a few days-long interruptions in operation due to maintenance. Previous studies show that HOx is most effective for preventing Mn release and promoting Mn removal when it is continuous and activated prior to the onset of stratification (Beutel and Horne, 1999; Debroux et al., 2012; Preece et al., 2019).

5 Conclusions

Our laboratory experiments confirm that Mn removal proceeds slowly in oxic waters at neutral to slightly alkaline pH (6-8) found in many freshwater bodies. However, conditions of high pH (10), which can occur during algal blooms, can result in rapid abiotic Mn removal. Increasing alkalinity concentrations above 70 mg/L $CaCO_3$ in addition to high pH promotes faster Mn removal than under high pH conditions alone. Analyses using SEM, EPMA and TEM are consistent with our interpretation of Mn oxidation as the primary mechanism of removal. Our results also suggest Mn oxides formed by initial Mn oxidation likely contributed to further Mn removal through adsorption of Mn(II) and/or heterogenous oxidation.

Experiments using water collected from FCR and CCR demonstrate the importance of mineral particles for promoting Mn removal. Analyses of particles formed in reservoir water experiments show close associations between Mn oxide and aluminosilicate or silicate minerals. This observation suggests that quartz or clay minerals present in the reservoir water column can facilitate Mn removal via adsorption of Mn followed by heterogenous Mn oxidation on the mineral surface. Overall, our experimental results shed light on the important role that suspended minerals in water bodies can play in driving Mn removal.

The kinetics of Mn oxidation are sensitive to background environmental conditions such as water geochemistry and the composition and density of suspended particles. Compared to in-situ treatment for more readily oxidized metals such as Fe, deploying and successfully employing HOx for Mn requires additional consideration because rates of Mn oxidation vary widely depending on geochemical drivers. For example, HOx for optimal control over Mn accumulation in the water column may require year-round operation in environments less

favorable to rapid Mn oxidation. We propose that comparisons of background Mn oxidation rates in a lake or reservoir could be used to determine the water body's suitability for HOx and the optimal HOx operation schedule.

Acknowledgements: Funding for this project was provided by the Virginia Tech Multicultural Academic Opportunities Program Graduate Fellowship, the Geological Society of America Graduate Research Grant Program, the Virginia Water Resources Research Center, the Roy J. Shlemon Scholarship from the Geological Society of America Environmental & Engineering Geology Division, the Virginia Tech Graduate and Professional Student Senate Graduate Research Development Program, the American Geosciences Institute Wallace Scholarship, NanoEarth at Virginia Tech, and the National Science Foundation (DEB-1753639, CNS-1737424, DBI-1933016). In addition, this work used shared facilities at the Virginia Tech National Center for Earth and Environmental Nanotechnology Infrastructure (NanoEarth), a member of the National Nanotechnology Coordinated Infrastructure, supported by NSF (ECCS 1542100 and ECCS 2025151).

We thank the Western Virginia Water Authority for allowing access to Falling Creek Reservoir and Carvins Cove Reservoir for sampling and monitoring. We appreciate the analytical support of Jeff Parks (ICP-MS), Ethan Frederick (ICP-OES) Kelly Peeler (IC), Lowell Moore (EPMA and SEM) and Sheri Singerling (TEM). The Virginia Tech Reservoir Group made invaluable contributions to fieldwork at the reservoirs and provided key feedback on this work. Gavin Moore assisted with laboratory sampling and experimental setup for the 14-day experiments. We greatly appreciate comments and input from Dr. Cayelan Carey, Dr. Benjamin Gill and Dr. F. Marc Michel.

Data Availability: Data reported in this manuscript are published in the Environmental Data Initiative repository (Carey et al., 2024; Ming and Schreiber, 2023; Schreiber et al., 2023).

References

Adams, J. P., Kirst, R., Kearns, L. E., and Krekeler, M. P., 2009, Mn-oxides and sequestration of heavy metals in a suburban catchment basin of the Chesapeake Bay watershed: Environmental Geology, v. 58, p. 1269-1280.

Austin, D., Scharf, R., Chen, C.-F., and Bode, J., 2019, Hypolimnetic oxygenation and aeration in two Midwestern USA reservoirs: Lake and Reservoir Management, v. 35, no. 3, p. 266-276.

Bargar, J. R., Tebo, B. M., and Villinski, J. E., 2000, In situ characterization of Mn(II) oxidation by spores of the marine Bacillus sp. strain SG-1: Geochimica et Cosmochimica Acta, v. 64, no. 16, p. 2775-2778.

Belitz, K., Fram, M. S., Lindsey, B. D., Stackelberg, P. E., Bexfield, L. M., Johnson, T. D., Jurgens, B. C., Kingsbury, J. A., McMahon, P. B., and Dubrovsky, N. M., 2022, Quality of Groundwater Used for Public Supply in the Continental United States: A Comprehensive Assessment: ACS ES&T Water, v. 2, no. 12, p. 2645-2656.

Bethke, C. M., 2022, Geochemical and biogeochemical reaction modeling, Cambridge University Press.

Beutel, M. W., and Horne, A. J., 1999, A review of the effects of hypolimnetic oxygenation on lake and reservoir water quality: Lake and Reservoir Management, v. 15, no. 4, p. 285-297.

Bouchard, M. F., Sauve, S., Barbeau, B., Legrand, M., Brodeur, M. E., Bouffard, T., Limoges, E., Bellinger, D. C., and Mergler, D., 2011, Intellectual Impairment in School-Age Children Exposed to Manganese from Drinking Water: Environmental Health Perspectives, v. 119, no. 1, p. 138-143.

Bryant, L. D., Hsu-Kim, H., Gantzer, P. A., and Little, J. C., 2011, Solving the problem at the source: Controlling Mn release at the sediment-water interface via hypolimnetic oxygenation: Water Research, v. 45, no. 19, p. 6381-6392.

Carey, C. C., Hanson, P. C., Thomas, R. Q., Gerling, A. B., Hounshell, A. G., Lewis, A. S., Lofton, M. E., McClure, R. P., Wander, H. L., and Woelmer, W. M., 2022, Anoxia decreases the magnitude of the carbon, nitrogen, and phosphorus sink in freshwaters: Global Change Biology, v. 28, no. 16, p. 4861-4881.

Carey, C. C., Lewis, A. S., and Breef-Pilz, A., 2024, Time series of high-frequency profiles of depth, temperature, dissolved oxygen, conductivity, specific conductance, chlorophyll a, turbidity, pH, oxidation-reduction potential, photosynthetically active radiation, colored dissolved organic matter, phycocyanin, phycoerythrin, and descent rate for Beaverdam Reservoir, Carvins Cove Reservoir, Falling Creek Reservoir, Gatewood Reservoir, and Spring Hollow Reservoir in southwestern Virginia, USA 2013-2023 ver 14. , *in* Environmental Data Initiative, ed.: https://doi.org/10.6073/pasta/b406e9a104dafb1b91e1ad85a19384db.

Cerrato, J. M., Falkinham, J. O., Dietrich, A. M., Knocke, W. R., McKinney, C. W., and Pruden, A., 2010, Manganese-oxidizing and -reducing microorganisms isolated from biofilms in chlorinated drinking water systems: Water Research, v. 44, no. 13, p. 3935-3945.

Chapnick, S. D., Moore, W. S., and Nealson, K. H., 1982, Microbially mediated manganese oxidation in a freshwater lake: Limnology and Oceanography, v. 27, no. 6, p. 1004-1014.

Cheng, H., Yang, T., Jiang, J., Lu, X., Wang, P., and Ma, J., 2020a, Mn^{2+} effect on manganese oxides (MnOx) nanoparticles aggregation in solution: chemical adsorption and cation bridging: Environmental Pollution, v. 267, p. 115561.

Cheng, Y., Xiong, W., and Huang, T., 2020b, Catalytic oxidation removal of manganese from groundwater by iron–manganese co-oxide filter films under anaerobic conditions: Science of The Total Environment, v. 737, p. 139525.
Davies, S. H., and Morgan, J. J., 1989, Manganese (II) oxidation kinetics on metal oxide surfaces: Journal of Colloid and Interface Science, v. 129, no. 1, p. 63-77.
Davison, W., 1993, Iron and manganese in lakes: Earth-Science Reviews, v. 34, no. 2, p. 119-163.
De Vitre, R. R., and Davison, W., 1993, Manganese particles in freshwaters, Environmental Particles, Volume 2, CRC Press, p. 317.
Debroux, J.-F., Beutel, M. W., Thompson, C. M., and Mulligan, S., 2012, Design and testing of a novel hypolimnetic oxygenation system to improve water quality in Lake Bard, California: Lake and Reservoir Management, v. 28, no. 3, p. 245-254.
Dent, S. R., Beutel, M. W., Gantzer, P., and Moore, B. C., 2014, Response of methylmercury, total mercury, iron and manganese to oxygenation of an anoxic hypolimnion in North Twin Lake, Washington: Lake and Reservoir Management, v. 30, no. 2, p. 119-130.
Diem, D., and Stumm, W., 1984, Is dissolved Mn^{2+} being oxidized by O_2 in absence of Mn-bacteria or surface catalysts?: Geochimica et Cosmochimica Acta, v. 48, no. 7, p. 1571-1573.
Downs, R. T., and Hall-Wallace, M., 2003, The American Mineralogist crystal structure database: American Mineralogist, v. 88, no. 1, p. 247-250.
Eaton, A., 2021, Assessment of Manganese Occurrence in Drinking Water in the United States: ACS ES&T Water, v. 1, no. 11, p. 2450-2458.
Elzinga, E. J., 2011, Reductive Transformation of Birnessite by Aqueous Mn(II): Environmental Science & Technology, v. 45, no. 15, p. 6366-6372.
Elzinga, E. J., 2016, ^{54}Mn radiotracers demonstrate continuous dissolution and reprecipitation of vernadite (δ-MnO_2) during interaction with aqueous Mn (II): Environmental Science & Technology, v. 50, no. 16, p. 8670-8677.
Friedl, G., Wehrli, B., and Manceau, A., 1997, Solid phases in the cycling of manganese in eutrophic lakes: New insights from EXAFS spectroscopy: Geochimica et Cosmochimica Acta, v. 61, no. 2, p. 275-290.
Gantzer, P. A., Bryant, L. D., and Little, J. C., 2009a, Controlling soluble iron and manganese in a water-supply reservoir using hypolimnetic oxygenation: Water Research, v. 43, no. 5, p. 1285-1294.
Gantzer, P. A., Bryant, L. D., and Little, J. C., 2009b, Effect of hypolimnetic oxygenation on oxygen depletion rates in two water-supply reservoirs: Water Research, v. 43, no. 6, p. 1700-1710.
Gerling, A. B., Browne, R. G., Gantzer, P. A., Mobley, M. H., Little, J. C., and Carey, C. C., 2014, First report of the successful operation of a side stream supersaturation hypolimnetic oxygenation system in a eutrophic, shallow reservoir: Water Research, v. 67, p. 129-143.
Gillispie, E. C., Austin, R. E., Rivera, N. A., Bolich, R., Duckworth, O. W., Bradley, P., Amoozegar, A., Hesterberg, D., and Polizzotto, M. L., 2016, Soil weathering as an engine for manganese contamination of well water: Environmental Science & Technology, v. 50, no. 18, p. 9963-9971.
Godwin, C. M., Zehnpfennig, J. R., and Learman, D. R., 2020, Biotic and abiotic mechanisms of manganese (II) oxidation in Lake Erie: Frontiers in Environmental Science, v. 8, p. 57.

Hamilton-Taylor, J., Davison, W., and Morfett, K., 1996, The biogeochemical cycling of Zn, Cu, Fe, Mn, and dissolved organic C in a seasonally anoxic lake: Limnology and Oceanography, v. 41, no. 3, p. 408-418.
Hem, J. D., 1963, Chemical equilibria and rates of manganese oxidation, US Government printing office, Water Supply Paper USGS Numbered Series, v. 1667.
Hem, J. D., and Lind, C. J., 1983, Nonequilibrium models for predicting forms of precipitated manganese oxides: Geochimica et Cosmochimica Acta, v. 47, no. 11, p. 2037-2046.
Herndon, E. M., Havig, J. R., Singer, D. M., McCormick, M. L., and Kump, L. R., 2018, Manganese and iron geochemistry in sediments underlying the redox-stratified Fayetteville Green Lake: Geochimica et Cosmochimica Acta, v. 231, p. 50-63.
Heu, R., Shahbazmohamadi, S., Yorston, J., and Capeder, P., 2019, Target material selection for sputter coating of SEM samples: Microscopy Today, v. 27, no. 4, p. 32-36.
Hotze, E. M., Phenrat, T., and Lowry, G. V., 2010, Nanoparticle aggregation: challenges to understanding transport and reactivity in the environment: Journal of Environmental Quality, v. 39, no. 6, p. 1909-1924.
Hsiung, T.-M., and Tisue, T., 1994, Manganese Dynamics in Lake Richard B. Russell, ACS Publications.
Junta, J. L., and Hochella Jr, M. F., 1994, Manganese (II) oxidation at mineral surfaces: A microscopic and spectroscopic study: Geochimica et Cosmochimica Acta, v. 58, no. 22, p. 4985-4999.
Kohl, P. M., and Medlar, S. J., 2006, Occurrence of manganese in drinking water and manganese control, Denver CO, American Water Works Association.
Krueger, K. M., Vavrus, C. E., Lofton, M. E., McClure, R. P., Gantzer, P., Carey, C. C., and Schreiber, M. E., 2020, Iron and manganese fluxes across the sediment-water interface in a drinking water reservoir: Water Research, v. 182, p. 116003.
Lan, S., Wang, X., Xiang, Q., Yin, H., Tan, W., Qiu, G., Liu, F., Zhang, J., and Feng, X., 2017, Mechanisms of Mn (II) catalytic oxidation on ferrihydrite surfaces and the formation of manganese (oxyhydr) oxides: Geochimica et Cosmochimica Acta, v. 211, p. 79-96.
Learman, D., Wankel, S., Webb, S., Martinez, N., Madden, A., and Hansel, C. M., 2011, Coupled biotic–abiotic Mn (II) oxidation pathway mediates the formation and structural evolution of biogenic Mn oxides: Geochimica et Cosmochimica Acta, v. 75, no. 20, p. 6048-6063.
Lefkowitz, J. P., Rouff, A. A., and Elzinga, E. J., 2013, Influence of pH on the Reductive Transformation of Birnessite by Aqueous Mn(II): Environmental Science & Technology, v. 47, no. 18, p. 10364-10371.
Li, H., Santos, F., Butler, K., and Herndon, E., 2021, A Critical Review on the Multiple Roles of Manganese in Stabilizing and Destabilizing Soil Organic Matter: Environmental Science & Technology, v. 55, no. 18, p. 12136-12152.
Li, N., Huang, T., Mao, X., Zhang, H., Li, K., Wen, G., Lv, X., and Deng, L., 2019, Controlling reduced iron and manganese in a drinking water reservoir by hypolimnetic aeration and artificial destratification: Science of the Total Environment, v. 685, p. 497-507.
Madden, A. S., and Hochella Jr, M. F., 2005, A test of geochemical reactivity as a function of mineral size: Manganese oxidation promoted by hematite nanoparticles: Geochimica et Cosmochimica Acta, v. 69, no. 2, p. 389-398.

Man, X., Bierlein, K. A., Lei, C., Bryant, L. D., Wüest, A., and Little, J. C., 2020, Improved modeling of sediment oxygen kinetics and fluxes in lakes and reservoirs: Environmental Science & Technology, v. 54, no. 5, p. 2658-2666.

Ming, C. L., and Schreiber, M. E., 2023, Laboratory experiments testing pH, alkalinity and particle impacts on Mn removal ver 1., *in* Environmental Data Initiative, ed.: https://doi.org/10.6073/pasta/84fc50f3798a1b758e04570a98caaf55.

Moosdorf, N., Hartmann, J., and Dürr, H. H., 2010, Lithological composition of the North American continent and implications of lithological map resolution for dissolved silica flux modeling: Geochemistry, Geophysics, Geosystems, v. 11, no. 11.

Morgan, J. J., 2005, Kinetics of reaction between O2 and Mn (II) species in aqueous solutions: Geochimica et Cosmochimica Acta, v. 69, no. 1, p. 35-48.

Munger, Z. W., Carey, C. C., Gerling, A. B., Hamre, K. D., Doubek, J. P., Klepatzki, S. D., McClure, R. P., and Schreiber, M. E., 2016, Effectiveness of hypolimnetic oxygenation for preventing accumulation of Fe and Mn in a drinking water reservoir: Water Research, v. 106, p. 1-14.

Neculita, C. M., and Rosa, E., 2019, A review of the implications and challenges of manganese removal from mine drainage: Chemosphere, v. 214, p. 491-510.

Oulhote, Y., Mergler, D., Barbeau, B., Bellinger, D. C., Bouffard, T., Brodeur, M.-È., Saint-Amour, D., Legrand, M., Sauvé, S., and Bouchard, M. F., 2014, Neurobehavioral function in school-age children exposed to manganese in drinking water: Environmental Health Perspectives, v. 122, no. 12, p. 1343-1350.

Post, J. E., 1999, Manganese oxide minerals: Crystal structures and economic and environmental significance: Proceedings of the National Academy of Sciences, v. 96, no. 7, p. 3447-3454.

Preece, E. P., Moore, B. C., Skinner, M. M., Child, A., and Dent, S., 2019, A review of the biological and chemical effects of hypolimnetic oxygenation: Lake and Reservoir Management, v. 35, no. 3, p. 229-246.

Putz, H., Brandenburg, K.,, n.d., Match! - Phase Analysis using Powder Diffraction, Version 3.x *in* Scientists, C. I. S. f., ed.: https://www.crystalimpact.de/match.

Rimstidt, J. D., 2014, Geochemical rate models: an introduction to geochemical kinetics, New York, Cambridge University Press.

Roland, J. V., 1970, Some effects of the introduction of hard water into Carvin Cove Reservoir, Virginia: Virginia Polytechnic Institute and State University.

Sánchez-España, J., and Yusta, I., 2019, Coprecipitation of Co^{2+}, Ni^{2+} and Zn^{2+} with Mn (III/IV) oxides formed in metal-rich mine waters: Minerals, v. 9, no. 4, p. 226.

Scholtysik, G., Dellwig, O., Roeser, P., Arz, H. W., Casper, P., Herzog, C., Goldhammer, T., and Hupfer, M., 2020, Geochemical focusing and sequestration of manganese during eutrophication of Lake Stechlin (NE Germany): Biogeochemistry, v. 151, no. 2-3, p. 313-334.

Schreiber, M. E., Ming, C. L., Hammond, N. W., Breef-Pilz, A., Geisler, B., and Haynie, G., 2023, Time series of total and soluble iron and manganese concentrations from Falling Creek Reservoir, Beaverdam Reservoir and Carvins Cove Reservoir in southwestern Virginia, USA from 2014 through 2022, *in* Environmental Data Initiative, ed.: https://doi.org/10.6073/pasta/9d901ae44871e018f475f42c58fb2004.

Semasinghe, C., and Rousso, B. Z., 2023, In-Lake Mechanisms for Manganese Control—A Systematic Literature Review: Sustainability, v. 15, no. 11, p. 8785.

Stroud Research Center, 2017, Model My Watershed: https://wikiwatershed.org/.
Tebo, B. M., Johnson, H. A., McCarthy, J. K., and Templeton, A. S., 2005, Geomicrobiology of manganese (II) oxidation: Trends in Microbiology, v. 13, no. 9, p. 421-428.
Thibault de Chanvalon, A., Luther, G. W., Estes, E. R., Necker, J., Tebo, B. M., Su, J., and Cai, W. J., 2023, Influence of manganese cycling on alkalinity in the redox stratified water column of Chesapeake Bay: Biogeosciences, v. 20, no. 14, p. 3053-3071.
Tipping, E., Thompson, D., and Davison, W., 1984, Oxidation products of Mn (II) in lake waters: Chemical Geology, v. 44, no. 4, p. 359-383.
Tobiason, J. E., Bazilio, A., Goodwill, J., Mai, X., and Nguyen, C., 2016, Manganese removal from drinking water sources: Current Pollution Reports, v. 2, p. 168-177.
Wasserman, G. A., Liu, X., Parvez, F., Factor-Litvak, P., Ahsan, H., Levy, D., Kline, J., van Geen, A., Mey, J., Slavkovich, V., Siddique, A. B., Islam, T., and Graziano, J. H., 2011, Arsenic and manganese exposure and children's intellectual function: Neurotoxicology, v. 32, no. 4, p. 450-457.
Western Virginia Water Authority, n.d., Historical Water Quality Data: Unpublished.
Wetzel, R. G., 2001, Limnology: Lake and River Ecosystems, 3rd edition, Academic Press, 1006 p.:
Williams, D. B., Carter, C. B., Williams, D. B., and Carter, C. B., 1996, The Transmission Electron Microscope: A Textbook for Materials Science, Boston, Springer.
Wilson, D. E., 1980, Surface and complexation effects on the rate of Mn (II) oxidation in natural waters: Geochimica et Cosmochimica Acta, v. 44, no. 9, p. 1311-1317.
Wittkop, C., Swanner, E. D., Grengs, A., Lambrecht, N., Fakhraee, M., Myrbo, A., Bray, A. W., Poulton, S. W., and Katsev, S., 2020, Evaluating a primary carbonate pathway for manganese enrichments in reducing environments: Earth and Planetary Science Letters, v. 538, p. 116201.
Woodward, H. P., 1932, Geology and mineral resources of the Roanoke area, Virginia, University, Virginia ;, Division of Purchase and Printing, Virginia Geological Survey. Bulletin 34.
World Health Organization, 2021, Manganese in drinking water: background document for development of WHO guidelines for drinking-water quality: World Health Organization.
Yang, Y., Liu, J., Zhu, R., Chen, Q., Wei, H., Chen, M., Xian, H., and He, H., 2023, Surface-induced oxidation of Mn(II) and crystallization of manganese (hydr)oxides on clay minerals: Geochimica et Cosmochimica Acta, v. 363, p. 129-146.
Zhang, F., Zhang, H., Bertone, E., Stewart, R., Shen, X., and Cinque, K., 2021, A three-dimensional manganese model for the management of a monomictic drinking water reservoir: Environmental Modelling & Software, v. 146, p. 105213.
Zhang, F., Zhang, H., Wang, X., Stewart, R. A., Bertone, E., Cinque, K., Jin, G., and Yuan, S., 2024, Effects of wind-driven current and thermal dynamics in a temperate monomictic reservoir: Implications for manganese transport and treatment in water supply systems: Journal of Environmental Management, v. 358, p. 120932.
Zhu, S., Ho, S.-H., Jin, C., Duan, X., and Wang, S., 2020, Nanostructured manganese oxides: natural/artificial formation and their induced catalysis for wastewater remediation: Environmental Science: Nano, v. 7, no. 2, p. 368-396.

Tables_Clean (Editable version)
Click here to access/download;Table (Editable version);240617_Tables_Clean.docx

Table 1. Summary of Mn removal mechanisms

Removal mechanism	Drivers	References
Abiotic oxidation by O_2	• Increased rate w/increased pH • Increased rate w/increased temperature	Davison (1993); Diem and Stumm (1984); Hem (1963)
Oxidation catalyzed by mineral surfaces (heterogeneous)	• Presence of minerals such as rhodochrosite, Fe oxides and hydroxides, Mn oxides and hydroxides	Davies and Morgan (1989); Diem and Stumm (1984); Junta and Hochella Jr (1994); Lan et al. (2017); Madden and Hochella Jr (2005); Yang et al. (2023)
Biotic oxidation	• Presence of Mn-oxidizers • Increased rate w/increased temperature	Chapnick et al. (1982); Friedl et al. (1997); Godwin et al. (2020); Tebo et al. (2005); Tipping et al. (1984)
Precipitation of Mn carbonates (non-redox)	• Elevated concentrations of carbonate or alkalinity • Higher pH	De Vitre and Davison (1993); Herndon et al. (2018); Wittkop et al. (2020); Thibault de Chanvalon et al. (2023)
Adsorption to minerals	• Presence of suspended minerals (Fe oxides, Mn oxides, clays) in water column	Godwin et al. (2020); Hsiung and Tisue (1994); Tipping et al. (1984); Lan et al. (2017)

Table 2: HOx system design and reservoir characteristics of Falling Creek Reservoir (Gerling et al., 2014) and Carvins Cove Reservoir (Gantzer et al., 2009; Man et al., 2020).

	Falling Creek Reservoir	Carvins Cove Reservoir
Maximum depth at full pond (m)	9.3	23
Surface area (km^2)	0.119	2.5
HOx system type	Side stream supersaturation	Linear diffuser
Depth of oxygen introduction (m)	8.5	~18
Designed daily oxygen input (kg/d)	25	Variable

Table 3: Initial pH and alkalinity for 14-day experiments

Trial	Initial pH	Initial alkalinity (mg/L $CaCO_3$)
High pH High alkalinity	10.5 ± 0.5	250 ± 100
Moderate pH Moderate alkalinity	7.5 ± 1*	70 ± 20
Moderate pH High alkalinity	8 ± 0.5*	250 ± 100
Circumneutral pH Low alkalinity	6.5*	20 ± 10
High pH Moderate alkalinity	10.5 ± 0.5	70 ± 20
High pH No added alkalinity	10.5 ± 0.5	20 ± 10
Moderate pH No added alkalinity	8 ± 0.5	5 ± 10*
Circumneutral pH No added alkalinity	6 ± 0.5*	2 ± 2

*estimated based on chemical principles and preliminary trials

Table 4: Initial pH and alkalinity for 24-hour experiments

Trial	Initial pH	Initial alkalinity (mg/L $CaCO_3$)
High pH High alkalinity	10.5 ± 0.5	250 ±100
High pH Moderate alkalinity	10.5 ± 0.5	70 ± 20
Neutral pH No added alkalinity	6 ± 0.5	2 ± 2

Figures_Clean
Click here to access/download;Figure;240617 Figures_Clean.docx

Figures

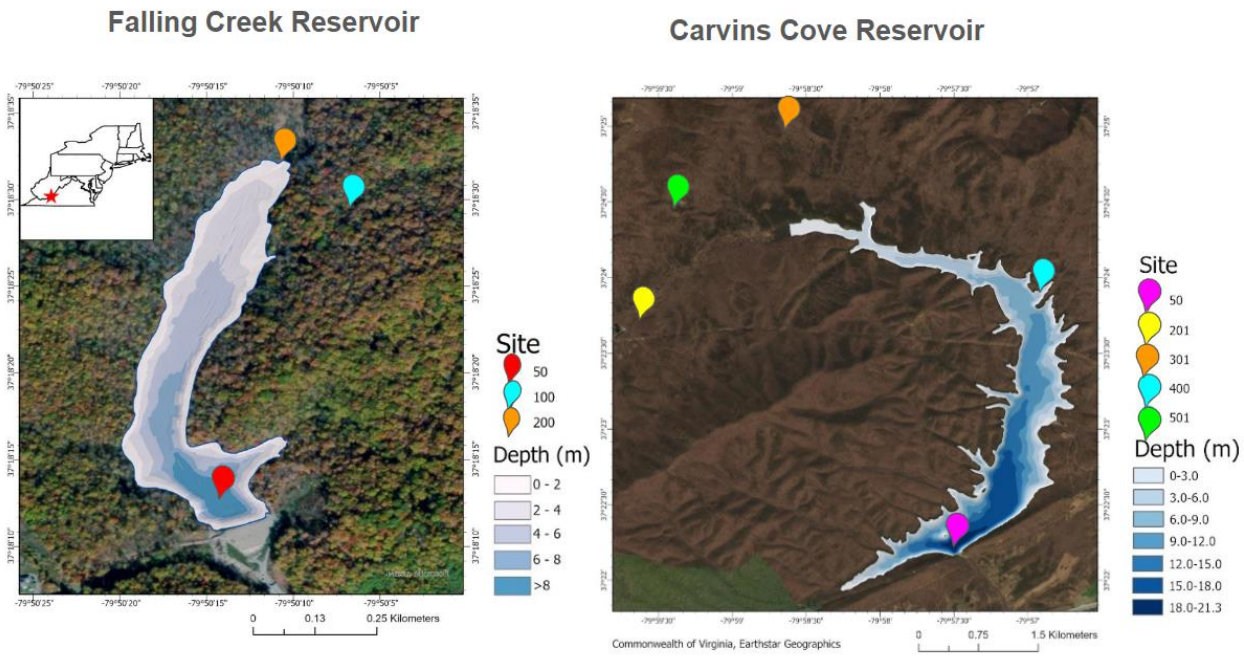

Figure 1. Site maps with location in Virginia in the inset. Map of Falling Creek Reservoir (FCR; left) overlaid on a reservoir bathymetric map. Water column sampling within FCR occurred at the deepest site (site 50). Site 100 and 200 are tributaries. Map of Carvins Cove Reservoir (CCR; right) overlaid on a reservoir bathymetric map. Water column sampling within CCR occurred at the deepest site (site 50). Sites 201, 301, 400, 501 are tributaries. Basemap imagery from Mazar, Commonwealth of Virginia and Earthstar Geographics.

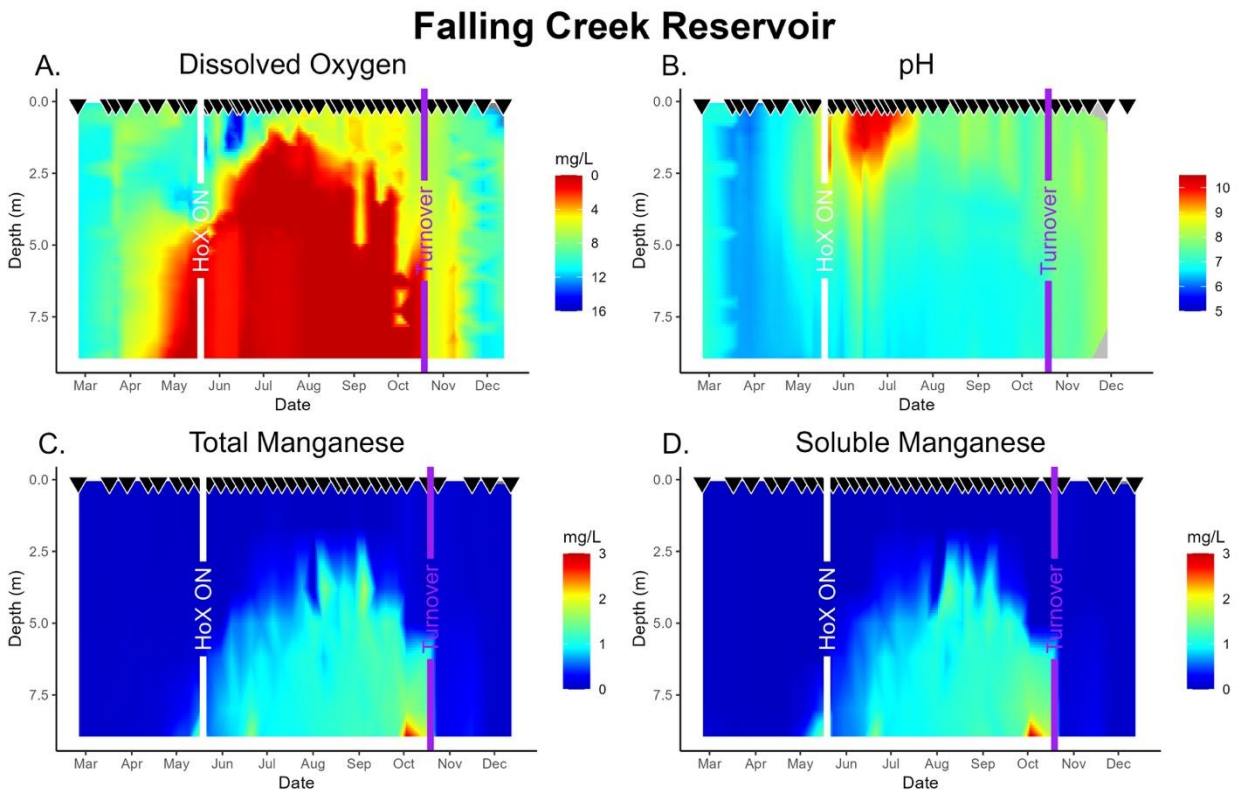

Figure 2. Heatmaps of water quality data from Falling Creek Reservoir in 2022, measured at site 50. A) dissolved oxygen, B) pH, C) total manganese and D) soluble manganese. Color scales show concentration gradations. White lines correspond to dates of HOx activation ("HOx on"). Purple lines correspond to reservoir turnover. Sampling dates show as inverted triangles at the top of each figure.

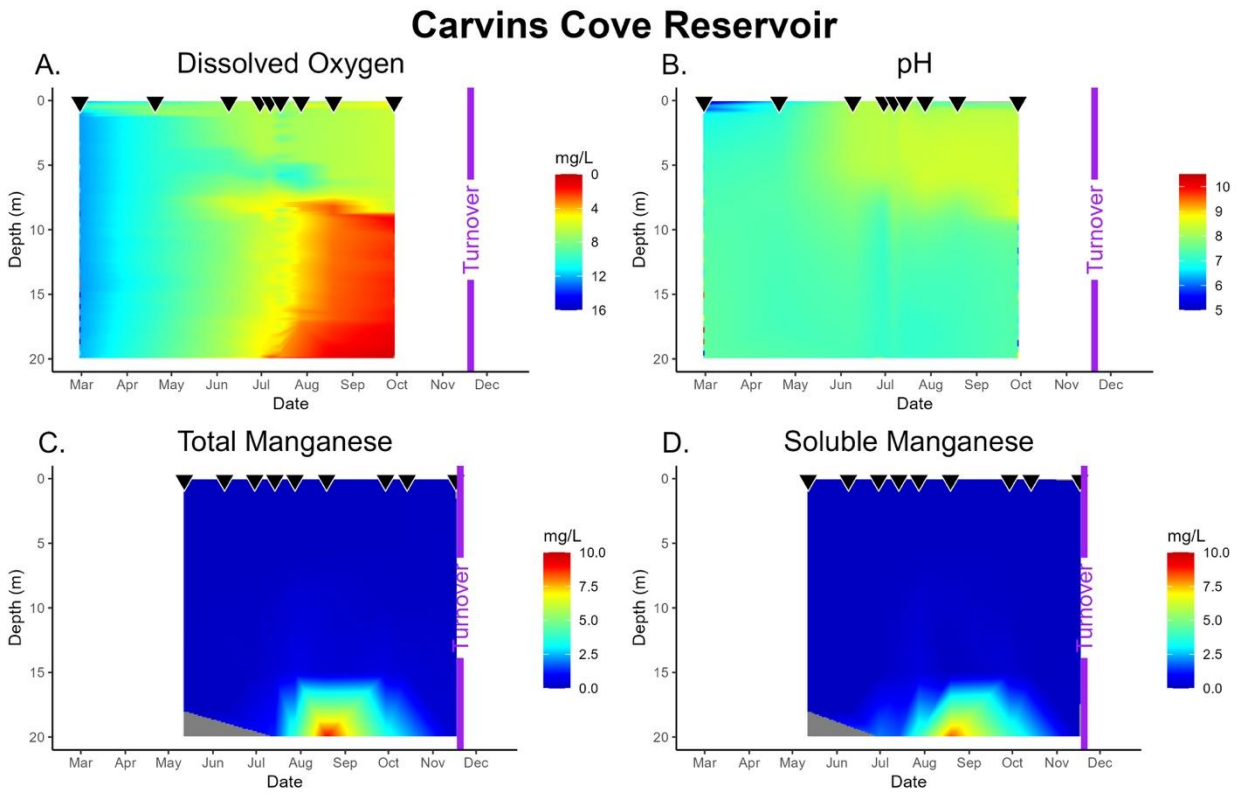

Figure 3. Heatmaps of water quality data from Carvins Creek Reservoir in 2022, measured at site 50. A) dissolved oxygen, B) pH, C) total manganese and D) soluble manganese. Color scales show concentration gradations. HOx was on for the entire 2022 season. Purple lines correspond to reservoir turnover. Sampling dates show as inverted triangles at the top of each figure.

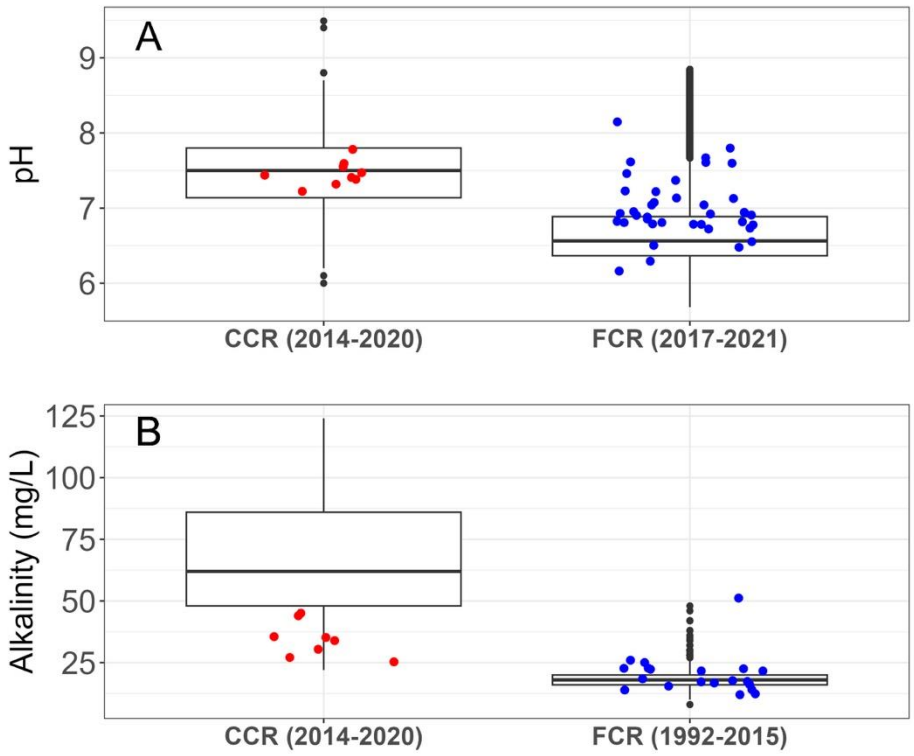

Figure 4. Boxplots of pH (A) and alkalinity (B; mg/L $CaCO_3$) for Carvins Cove Reservoir (CCR) and Falling Creek Reservoir (FCR). Historical data compiled from Western Virginia Water Authority monitoring data (Western Virginia Water Authority, n.d.), with 2022 data shown as red (CCR) or blue (FCR) dots.

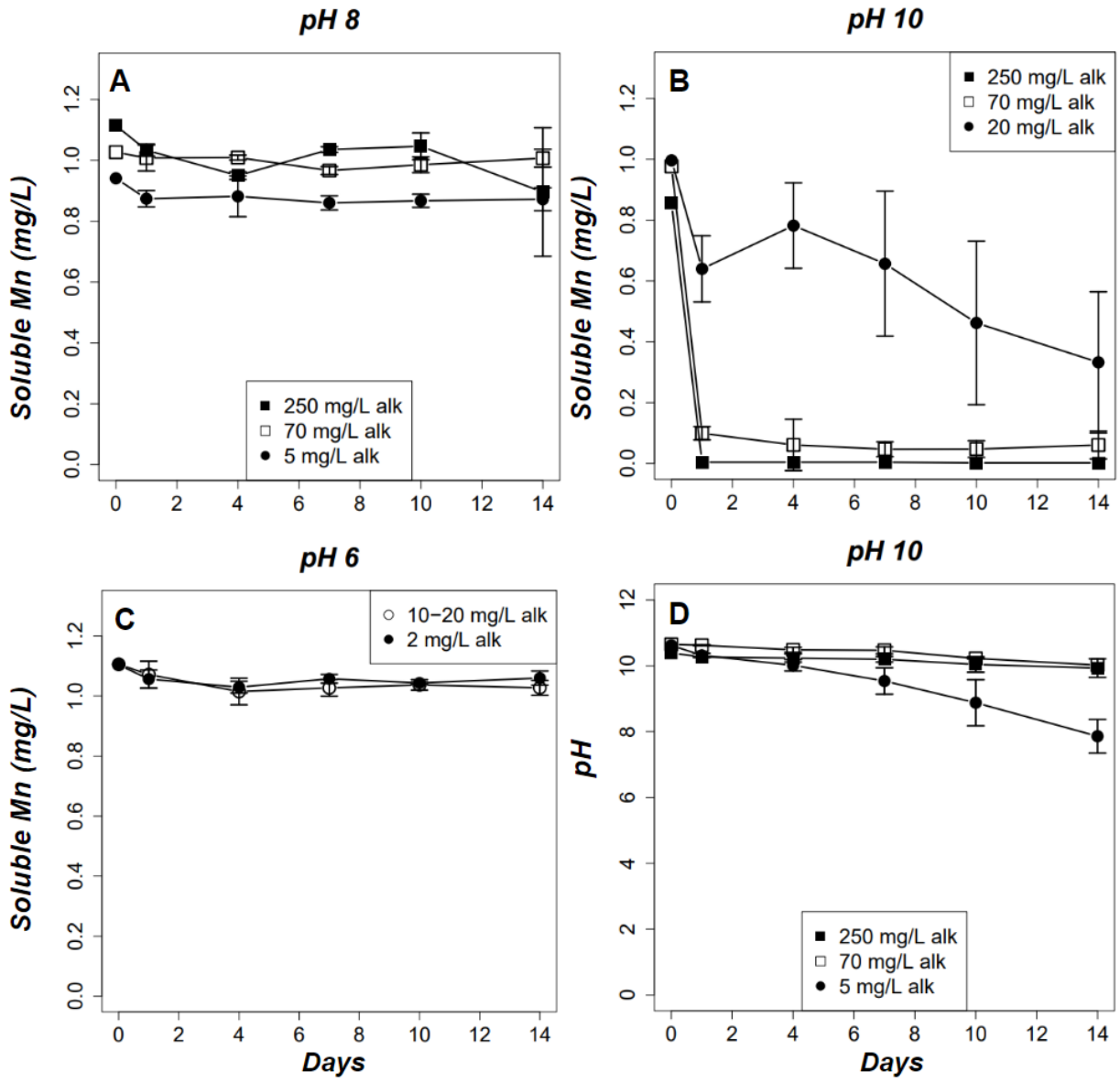

Figure 5. Soluble manganese (Mn, mg/L) concentrations and pH for 14-day experiments (see Table 3). Experiments were spiked with ~1 mg/L soluble Mn. Soluble Mn time series for pH 8 (A), pH10 (B), and pH 6 (C) experiments. D) pH time series for pH 10 experiments with different levels of alkalinity. Error bars reflect standard deviation from triplicate experiments. Alk = alkalinity in mg/L $CaCO_3$.

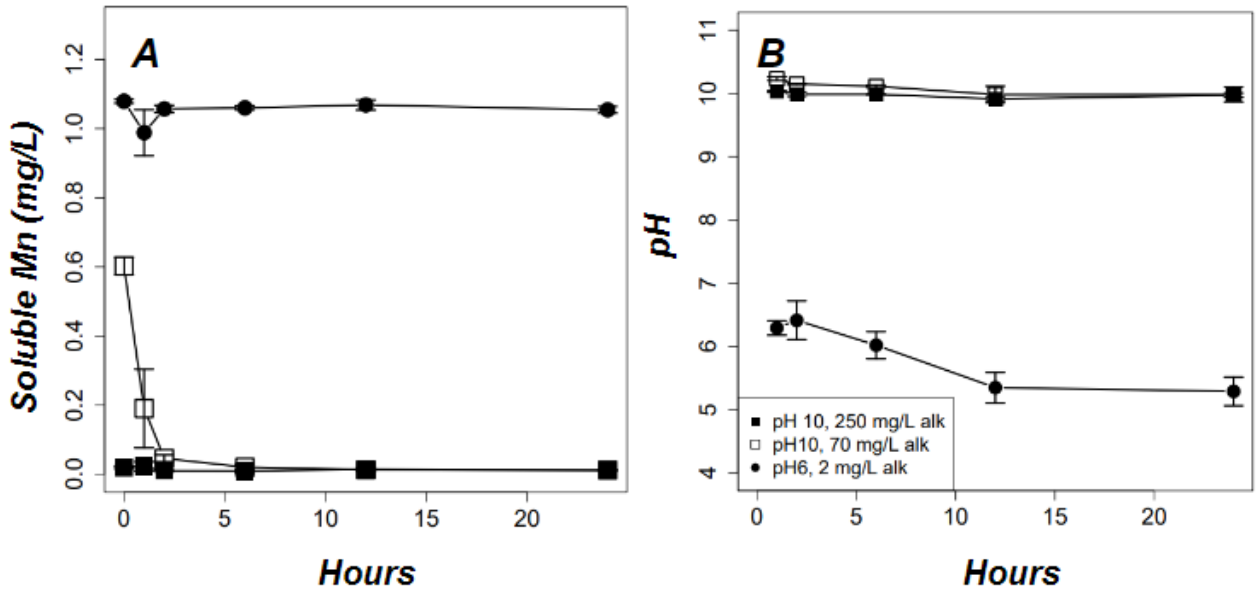

Figure 6. Soluble manganese (Mn; mg/L) concentrations (A) and pH (B) measured in 24-hour experiments (see Table 4). Experiments were spiked with ~1 mg/L soluble Mn. Error bars reflect standard deviation from triplicate experiments. Alk = alkalinity in mg/L $CaCO_3$

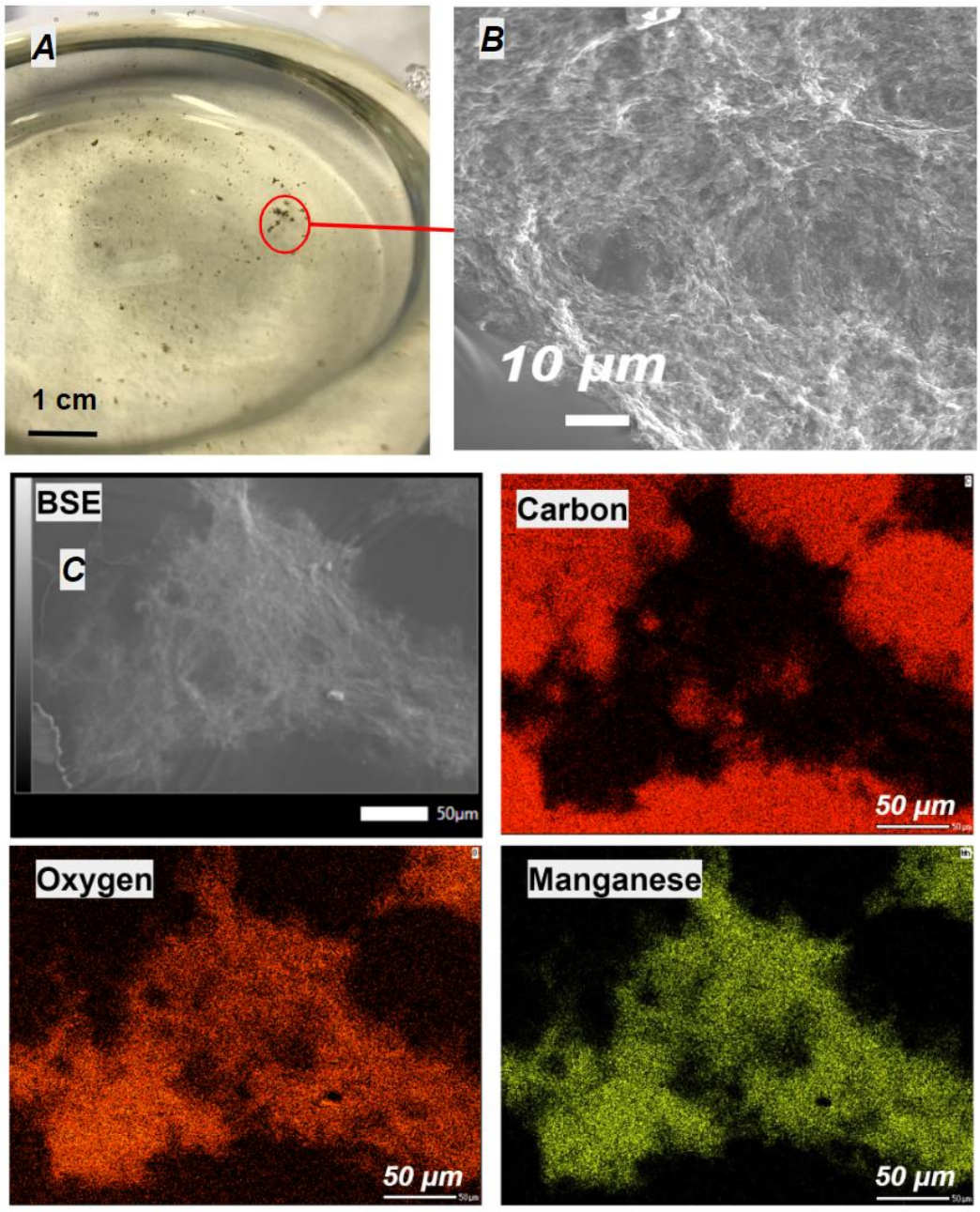

Figure 7. Scanning electron microscope (SEM) images and electron probe microanalysis (EPMA) maps of macroscopic (>100 µm) particles collected at 24 hours in pH 10 and 70 mg/L alkalinity solution. A) High pH/moderate alkalinity solution showing particles. B) Backscattered electron (BSE) image showing surface texture of macroscopic particles. C) Carbon, oxygen and manganese element maps of a representative macroscopic particle. Maps collected by EPMA, BSE image collected by SEM. Note that carbon surrounding the particle on the carbon map is from the mounting tape.

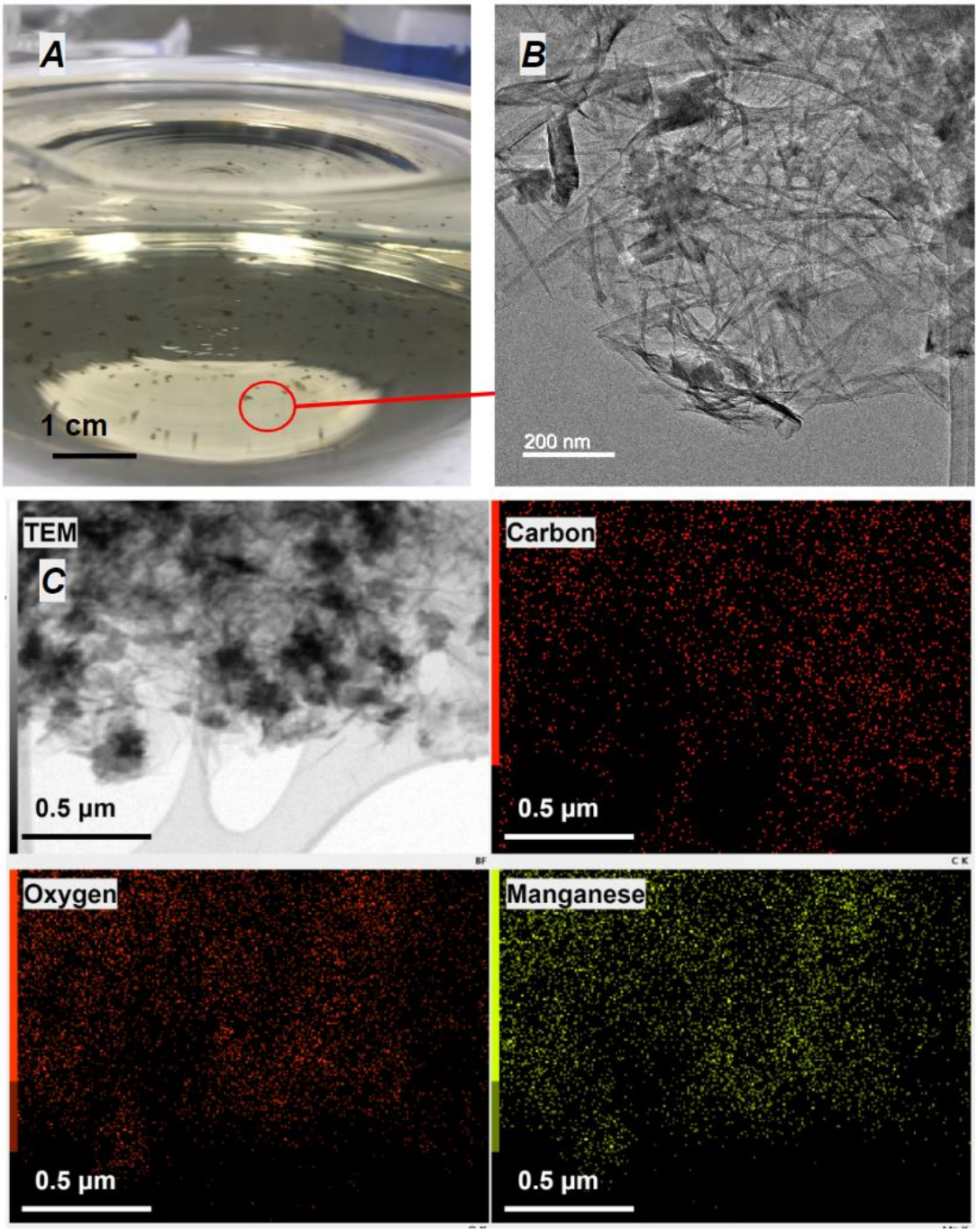

Figure 8. Transmission electron microscopy (TEM) images and energy dispersive spectroscopy (EDS) maps of microscopic (<5 µm) particles suspended in discolored pH 10 and 70 mg/L alkalinity solution. A) High pH/moderate alkalinity solution photographed at 12 hours. B) Brightfield TEM image showing aggregated needle-like crystals within micrometer-scale particles. C) Carbon, oxygen and manganese element TEM maps of the particle in B, shown at a different zoom of a different region of the particle. Maps collected by EDS. Carbon signal in element map likely introduced by lacy carbon grid.

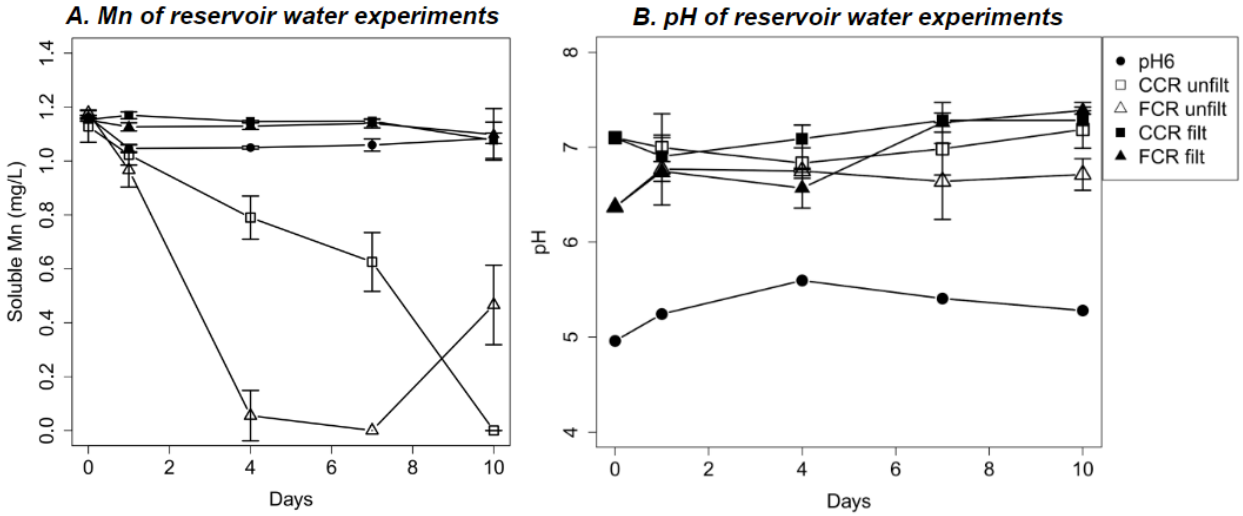

Figure 9. Soluble manganese (Mn; mg/L) concentrations (A) and pH (B) measured in FCR and CCR reservoir experiments. Experiments were spiked with ~1 mg/L soluble Mn. Error bars reflect standard deviation from triplicate experiments. Filtered reservoir water and control solutions were initially clear without any visible particles. In unfiltered reservoir water, tan and black silt to fine sand-sized particles were observed at hour 0. Unfiltered FCR water developed pink-orange discoloration between day 1-4, while unfiltered CCR water developed yellow-brown discoloration between day 4-7. In both unfiltered FCR and CCR water, particles were observed concomitant with discoloration.

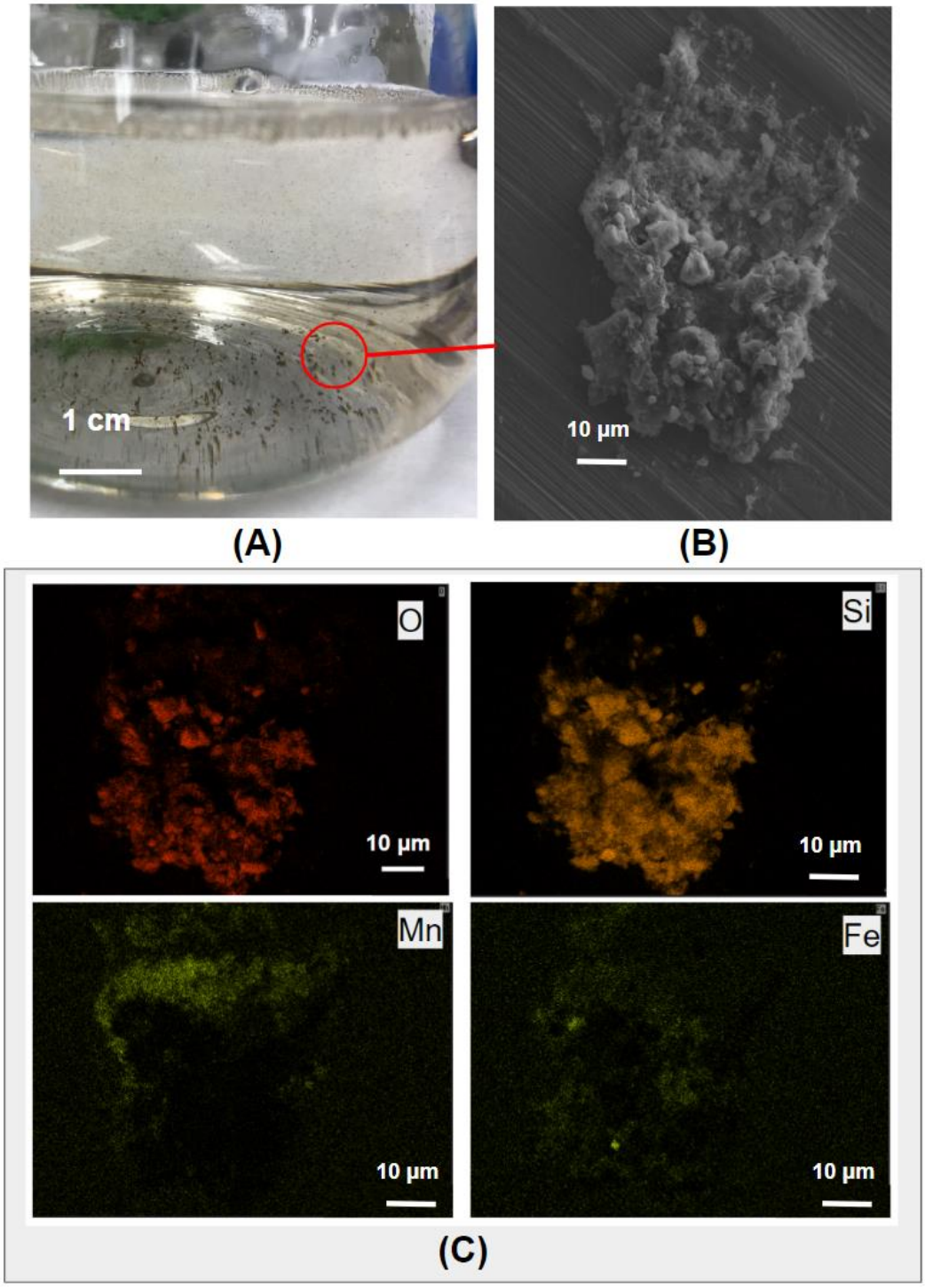

Figure 10. Falling Creek Reservoir (FCR) unfiltered reservoir water experiment showing macroscopic (>100 µm) particles in solution. A) Reservoir water photographed at 4 days. B) Scanning electron microscopy (SEM) of a particle collected at 10 days after Mn addition. C) Silicon, iron, oxygen and manganese element maps of the particle shown in B. Maps collected by EPMA.

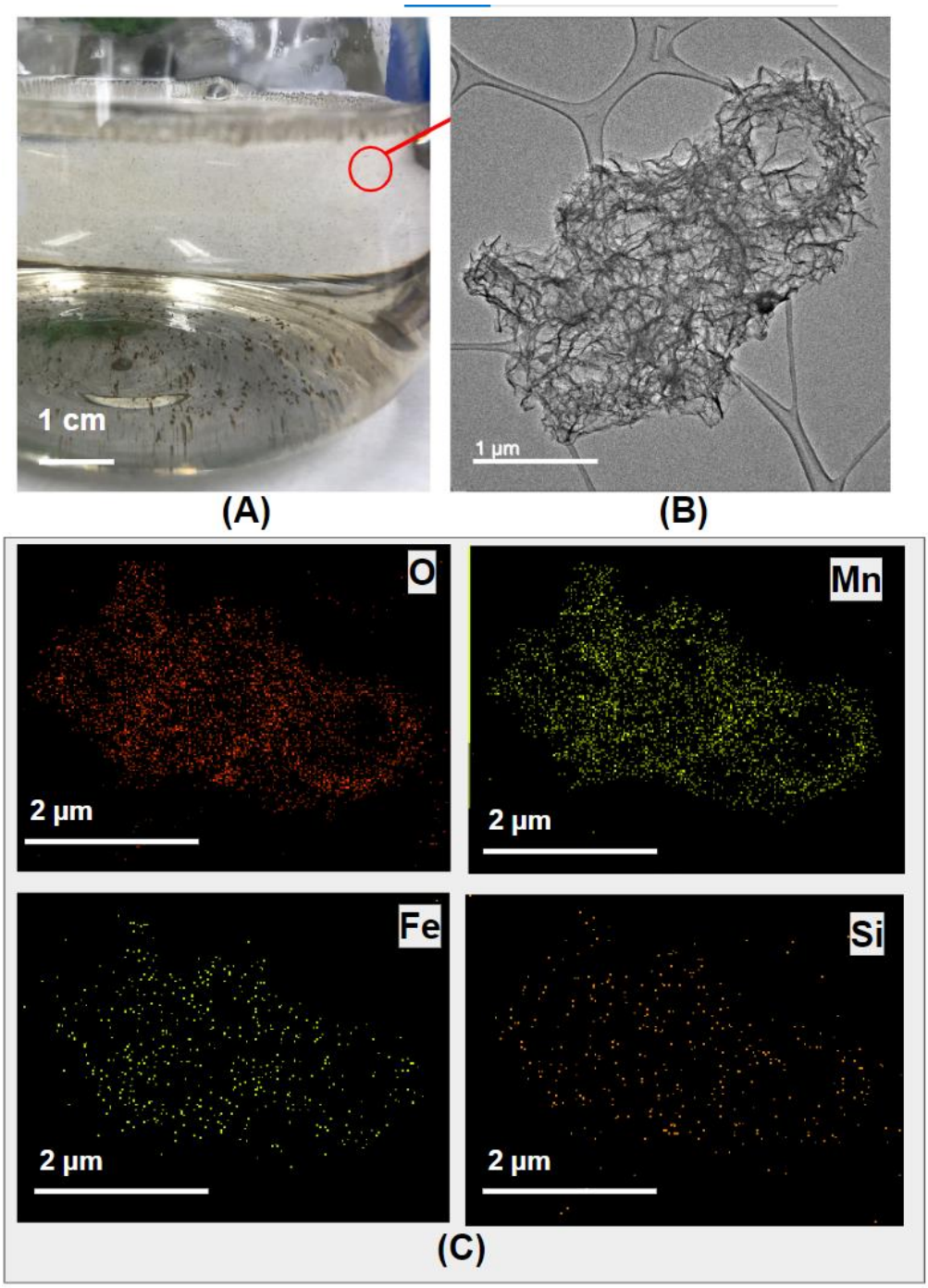

Figure 11. Falling Creek Reservoir (FCR) unfiltered reservoir water experiment showing discolored solution, which consists of microscopic (<5 µm) particles in solution. A) Reservoir water photographed at 4 days after Mn addition. B) Brightfield transmission electron microscopy (TEM) image of microscopic particle showing crumpled sheet particles suspended within discolored solution collected at 4 days. C) Energy-dispersive spectra (EDS) maps: Oxygen, manganese, iron and silicon element maps of the particle shown in B. Maps collected by energy-dispersive spectroscopy.

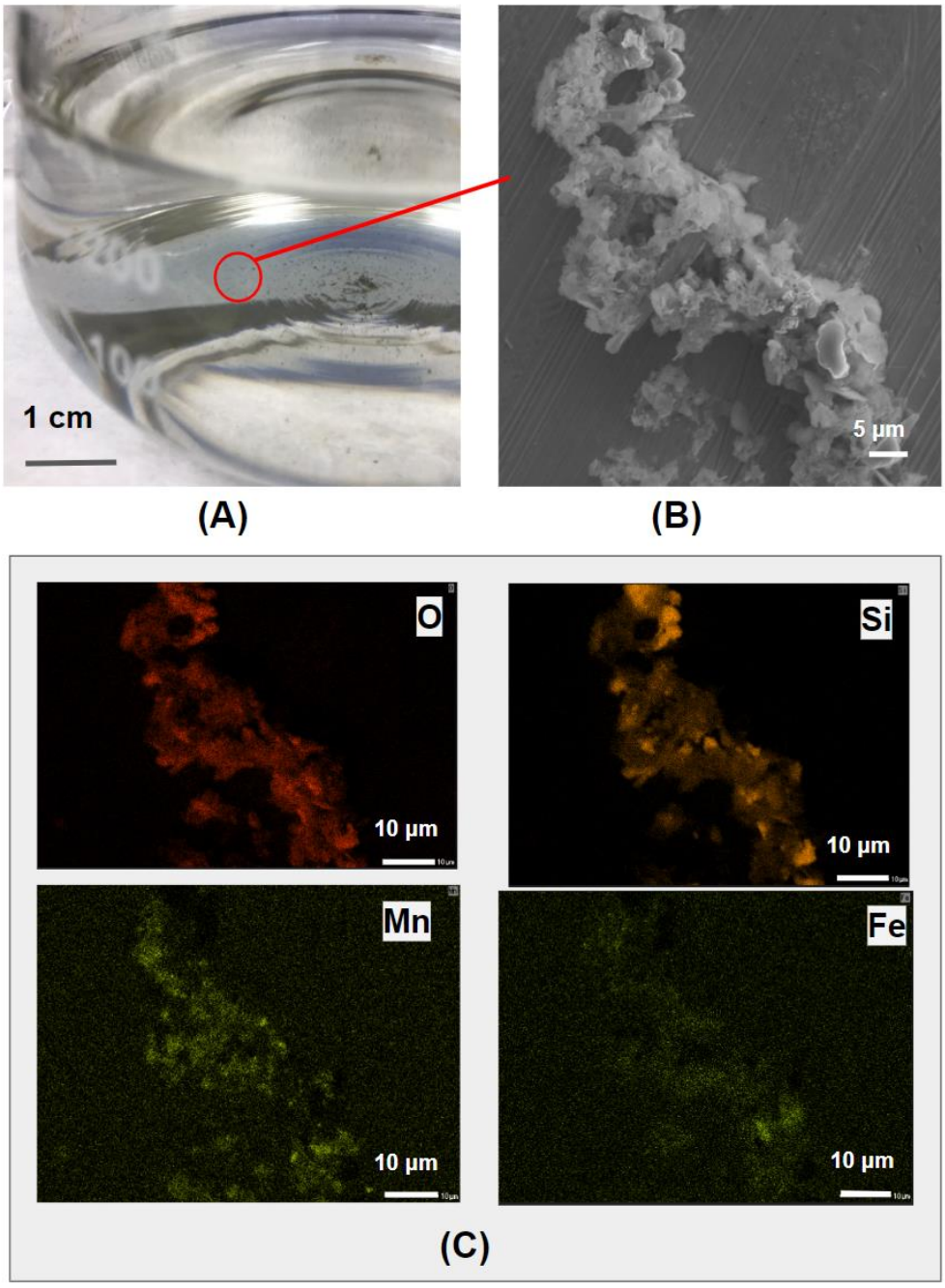

Figure 12. Carvins Cove Reservoir (CCR) unfiltered reservoir water experiment showing macroscopic particles in solution. A) Reservoir water photographed at 10 days. B) Scanning electron microscopy (SEM) of a macroscopic particle (>100 µm) collected at 10 days. C) Oxygen, silicon, manganese and iron element maps of the particle shown in B. Maps collected by EPMA.

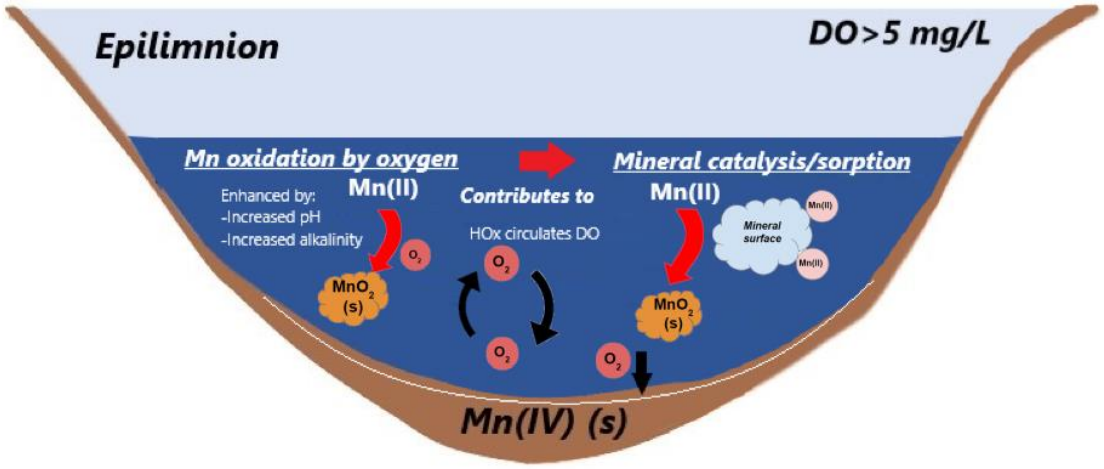

Figure 13. Conceptual model of Mn removal in drinking water reservoirs with hypolimnetic oxygenation. Removal can occur through multiple mechanisms, including oxidation by oxygen, sorption of Mn to mineral phases, and mineral catalysis (heterogenous oxidation). These mechanisms result in formation of Mn oxides, which settle to the bottom and become buried in sediment or reduced to soluble Mn during the next seasonal stratification.

Supplementary Material for

Ming et al. Geochemical drivers of manganese removal in drinking water reservoirs under hypolimnetic oxygenation

Submission to Applied Geochemistry

June 2024

Table S1: Falling Creek Reservoir and Carvins Cove Reservoir sampling site locations and descriptions.

Reservoir	Site	Description	Latitude	Longitude
CCR	50	Pelagic deep hole site of Carvins Cove Reservoir near dam; the closest access point to the dam via boat and 21 m at full pond	37.3706	-79.9582
CCR	201	Inflow stream site to Carvins Cove Reservoir at Carvins Creek Stream accessed via fire road near red barns	37.3958	-79.9937
CCR	301	Inflow stream site to Carvins Cove Reservoir at Sawmill Branch inflow site upstream of reservoir where fire road bridge crosses the stream	37.4169	-79.9771
CCR	400	Inflow tunnel site to Carvins Cove Reservoir at emergence of Tinker Creek Tunnel	37.399	-79.9485
CCR	501	Inflow tunnel site to Carvins Cove Reservoir at emergence of Catawba Creek Tunnel	37.4082	-79.9897
FCR	50	Pelagic deep hole site nearest to Falling Creek Reservoir dam; at end of FCR catwalk	37.30325	-79.8373
FCR	100	Inflow stream site on Tunnel Branch primary inflow to Falling Creek Reservoir; long-term monitoring site where gauged weir is located	37.30858	-79.83494
FCR	200	Inflow stream site on Falling Creek secondary inflow to Falling Creek Reservoir; also referred to as the wetland stream	37.30943	-79.83619

Table S2. Average alkalinity concentrations collected during the 2022 field season at Falling Creek Reservoir (FCR) and Carvins Cove Reservoir (CCR) at the surface (0.1 m) and the bottom of the reservoir (FCR at 9 m and CCR at 20 m)

Reservoir	Date	Depth (m)	Average alkalinity (mgL CaCO3)
FCR	6/7/2022	0.1	15.5
CCR	6/9/2022	0.1	25.25
FCR	6/27/2022	0.1	12.3
CCR	6/30/2022	0.1	27.15
CCR	6/30/2022	20	35.25
FCR	7/5/2022	0.1	17.25
FCR	7/5/2022	9	22.5
FCR	7/11/2022	0.1	16.1
FCR	7/11/2022	9	21.55
CCR	7/14/2022	0.1	35.625
CCR	7/14/2022	20	45.05
FCR	7/19/2022	0.1	17.15
FCR	7/19/2022	9	22.65
FCR	7/25/2022	0.1	16.85
FCR	7/25/2022	9	21.65
CCR	7/28/2022	0.1	30.5
CCR	7/28/2022	20	44.1
FCR	8/1/2022	0.1	14
FCR	8/1/2022	9	22.6
FCR	8/8/2022	0.1	18.35
FCR	8/8/2022	9	22.35
FCR	8/29/2022	0.1	14.05
FCR	8/29/2022	9	51.2
FCR	9/26/2022	0.1	12.1
FCR	9/26/2022	9	25.05
FCR	10/11/2022	0.1	17.75
FCR	10/11/2022	9	26.05
CCR	10/14/2022	0.1	33.85

Table S3: Reservoir pH, dissolved oxygen concentration and dissolved species concentrations input into Geochemist's Workbench software to calculate saturation indices. Concentrations that were below detection limit (BDL) set to 0.

Date (2022)	**6/7**	**6/7**	**6/7**	**6/7**	**6/7**	**6/7**	**6/7**	**7/11**	**7/11**	**7/11**	**7/11**	**7/11**	**7/11**	**7/11**	**7/14**	**7/14**	**7/14**	**7/14**	**7/14**	**7/14**
Reservoir	FCR	FCR	FCR	FCR	FCR	FCR	FCR	FCR	FCR	FCR	FCR	FCR	FCR	FCR	CCR	CCR	CCR	CCR	CCR	CCR
Depth (m)	0.1	1.6	3.8	5	6.2	8	9	0.1	1.6	3.8	5	6.2	8	9	0.1	1.5	6	9	15	20
Site	50	50	50	50	50	50	50	50	50	50	50	50	50	50	50	50	50	50	50	50
Cl (mg/L)	0.85	0.89	0.86	0.92	0.96	1.1	0.96	1.19	1	1.18	1.21	1.15	1.01	1.23	1.71	1.73	1.79	1.9	1.98	2.02
NO3-N (mg/L N)	0.1	0.1	0.1	0.1	0.1	0.1	0.1	0.1	0.1	0.1	0.1	0.1	0.1	0.1	0.1	0.1	0.1	0.1	0.1	0.1
SO4 (mg/L)	0.77	0.83	0.93	0.94	0.91	0.89	0.89	0.39	0.4	0.53	0.42	0.63	0.64	0.65	5.52	5.49	5.54	5.65	5.65	5.49
Na (ug/L)	2461	2535	2802	2958	2916	2963	2926	2603	2461	2797	2995	29340	2935	3038	1376	1396	1418	1460	1471	1476
Mg (ug/L)	860	894	1036	1130	1118	1154	1128	864	868	1051	1166	1160	1186	1184	2461	2505	2624	2808	2937	3012
Al (ug/L)	20	28	16	10	11	10	10	15	13	7	4	2	2	2	7	7	3	2	3	3
K (ug/L)	1042	1023	956	1000	1068	1086	1072	1279	1219	1243	1194	1224	1148	1312	910	921	927	939	947	979
Ca (ug/L)	1871	1909	2347	2675	2698	2773	2734	1894	1925	2588	2936	2918	2977	2991	9345	9449	9872	10637	11319	11593
Fe (ug/L)	248	267	138	51	56	42	43	617	576	1500	3496	352	39	69	6	BDL	BDL	BDL	BDL	13
Mn (ug/L)	3	3	3	416	581	680	634	24	32	358	764	860	959	942	1	6	1	61	221	1681
pH	9.67	9.65	8.26	7.83	7.42	7.12	6.99	9.23	8.26	7.18	7	6.82	6.64	6.6	8.26	8.33	8.22	7.69	7.23	7.11
DO (mg/L)	11.6	13.9	2.63	1.92	1.94	1.89	1.84	6.44	0.14	0.08	0.53	0.64	0.64	0.64	6.9	6.9	9.2	5.5	5.2	2.4
Alkalinity (mg/L $CaCO_3$)	15.5	15.5	15.5	15.5	15.5	15.5	15.5	16.1	16.1	16.1	21.55	21.55	21.55	21.55	35.63	35.63	45.5	45.5	45.5	45.5
Saturation Index (log Q/K)																				
Birnessite	39.1	38.2	48.7	59.6	54.2	50.0	47.6	51.7	53.01	-65.0	43.0	44.4	42.0	41.3	41.9	51.6	45.9	51.8	48.9	53
Hausmannite	2.9	2.5	6.9	11.0	9.0	7.4	6.6	7.8	9.5	-12	6.0	5.7	4.8	4.5	4.1	7.7	5.5	7.8	6.8	8.1
Rhodochrosite	-5.5	-5.6	-2.5	-0.71	-1.0	-1.2	-1.4	-3.3	-1.4	-1.5	-1.2	-1.4	-1.6	-1.6	-3.2	-2.1	-2.6	-1.3	-1.2	-0.4

Table S4: Qualitative observations of selected14-day experiment solutions.

Days	High pH/high alkalinity	High pH/moderate alkalinity
0	Clear	Clear
1	Clear solution with loose aggregated black-rusty brown particles	Yellow-brown discoloration
4	Clear solution with disaggregated black-rusty brown particles	Yellow-brown discoloration
7	Clear solution with aggregated black-rusty brown particles	Yellow-brown discoloration
10	Clear solution with aggregated black-rusty brown particles	Yellow-brown discoloration
14	Clear solution with aggregated black-rusty brown particles	Yellow-brown discoloration

Table S5: Mineral saturation indices for 14-day experiments. Calculations conducted using Geochemist's Workbench. See Table 3 for pH and alkalinity values. Experiments spiked with 1 mg/L Mn. Alk = alkalinity.

Treatment	high pH, moderate alk	high pH, high alk	high pH	moderate pH, moderate alk	moderate pH, high alk	moderate pH
Saturation Index (log Q/K)						
Birnessite	62.1	62.9	62.9	71.0	70.7	71.1
Hausmannite	12.3	12.4	12.4	15.2	15.2	15.4
Rhodochrosite	-2.0	-1.5	-2.3	1.2	1.2	-0.05

Table S6: Qualitative observations of 24-hour experimental solutions.

Hours	High pH/high alkalinity	High pH/moderate alkalinity	Control
0	Yellow-brown discoloration	Yellow-brown discoloration	Clear solution
1	Yellow-brown discoloration	Yellow-brown discoloration	Clear solution
2	Yellow-brown discoloration	Yellow-brown discoloration	Clear solution
6	Yellow-brown discoloration	Yellow-brown discoloration	Clear solution
12	Yellow-brown discoloration with reddish brown-black aggregates	Yellow-brown discoloration with reddish brown-black aggregates	Clear solution
24	Yellow-brown discoloration with reddish brown-black aggregates	Yellow-brown discoloration with reddish brown-black aggregates	Clear solution

Table S7: Qualitative observations of reservoir water experimental solutions.

Days	CCR unfiltered	FCR unfiltered	Control/FCR filtered/CCR filtered
0	Clear water with tan and black silt to sand sized particles	Clear water with tan and black silt to sand sized particles	Clear solution
1	Clear water with tan and black silt to sand sized particles	Clear water with tan and black silt to sand sized particles	Clear solution
4	Clear water with tan and black silt to sand sized particles	Pink-orange water with aggregated or silt-sized dispersed rusty brown to black particles	Clear solution
7	Slight brown-yellow discoloration of water with silt-sized dispersed brown to black particles	Pink-orange water with aggregated or silt-sized dispersed rusty brown to black particles	Clear solution
10	Slight brown-yellow discoloration of water with silt-sized dispersed brown to black particles	Pink-orange water with aggregated or silt-sized dispersed rusty brown to black particles	Clear solution

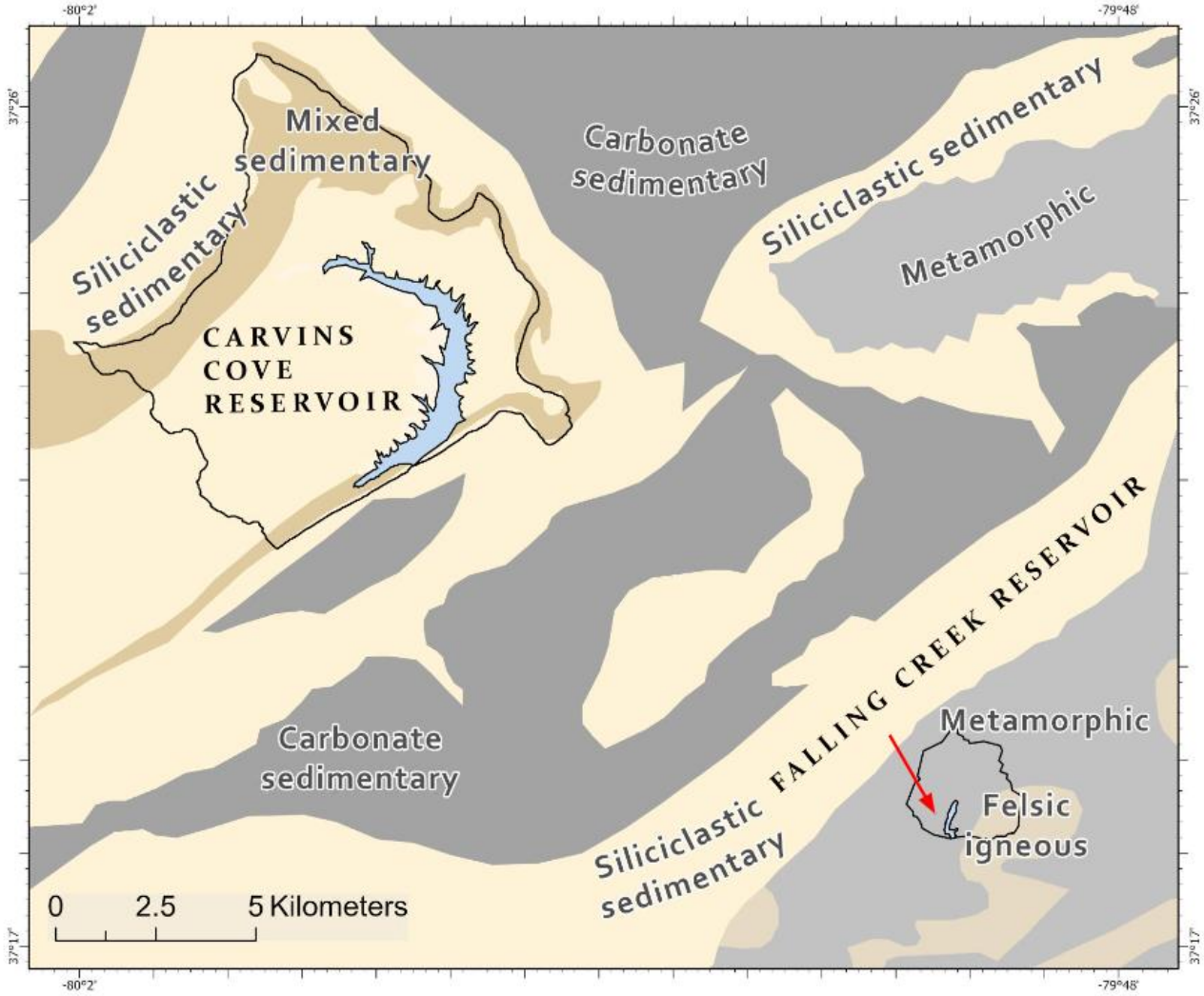

Figure S1: Bedrock lithology underlying the drainage basins of Falling Creek Reservoir (FCR) and Carvins Cove Reservoir (CCR). Reservoir watersheds are outlined in black. Watershed boundaries were obtained from Carey et al. (2022b). Lithology data from Moosdorf et al. (2010).

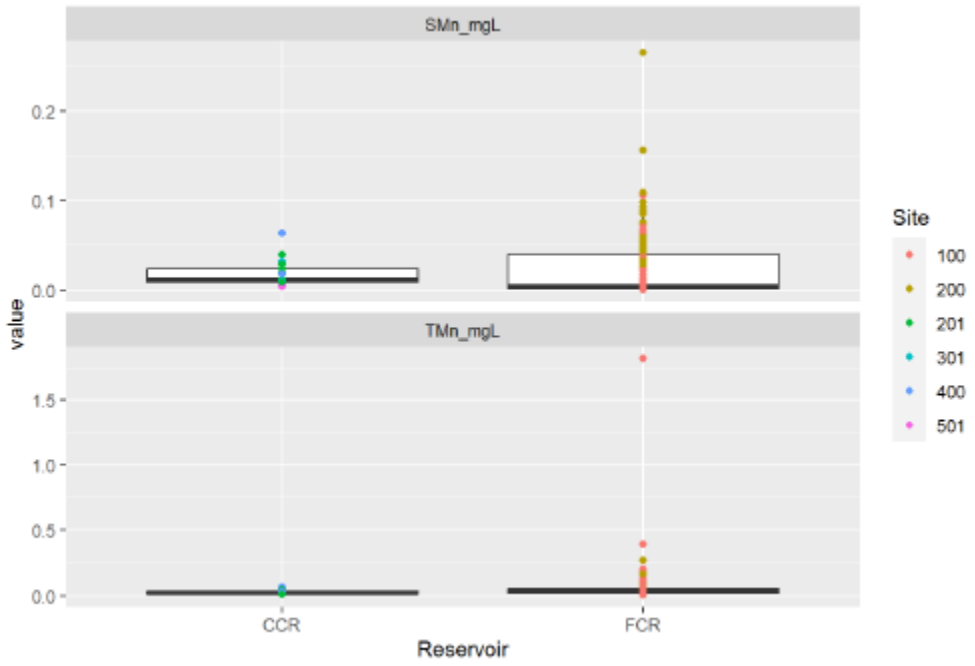

Figure S2. Soluble (top) and total (bottom) Mn concentrations in CCR and FCR tributaries in 2022. See locations of sites in Figure 1.

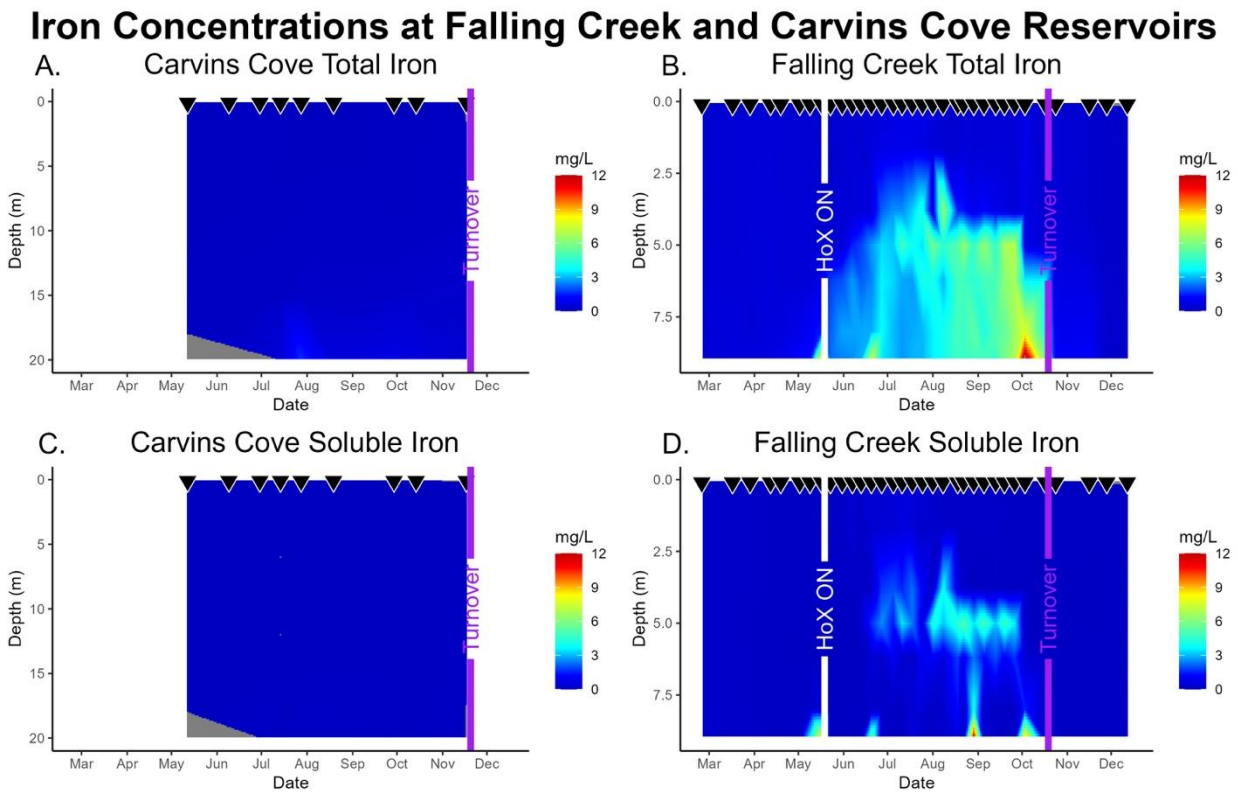

Figure S3. Heatmaps of soluble and total Fe from FCR and CCR in 2022, measured at site 50. Color scales show concentration gradations. White lines show date of HOx activated in FCR; the HOx was on for the entire 2022 season in CCR. Purple lines correspond to reservoir turnover. Sampling dates show as inverted triangles at the top of each figure.

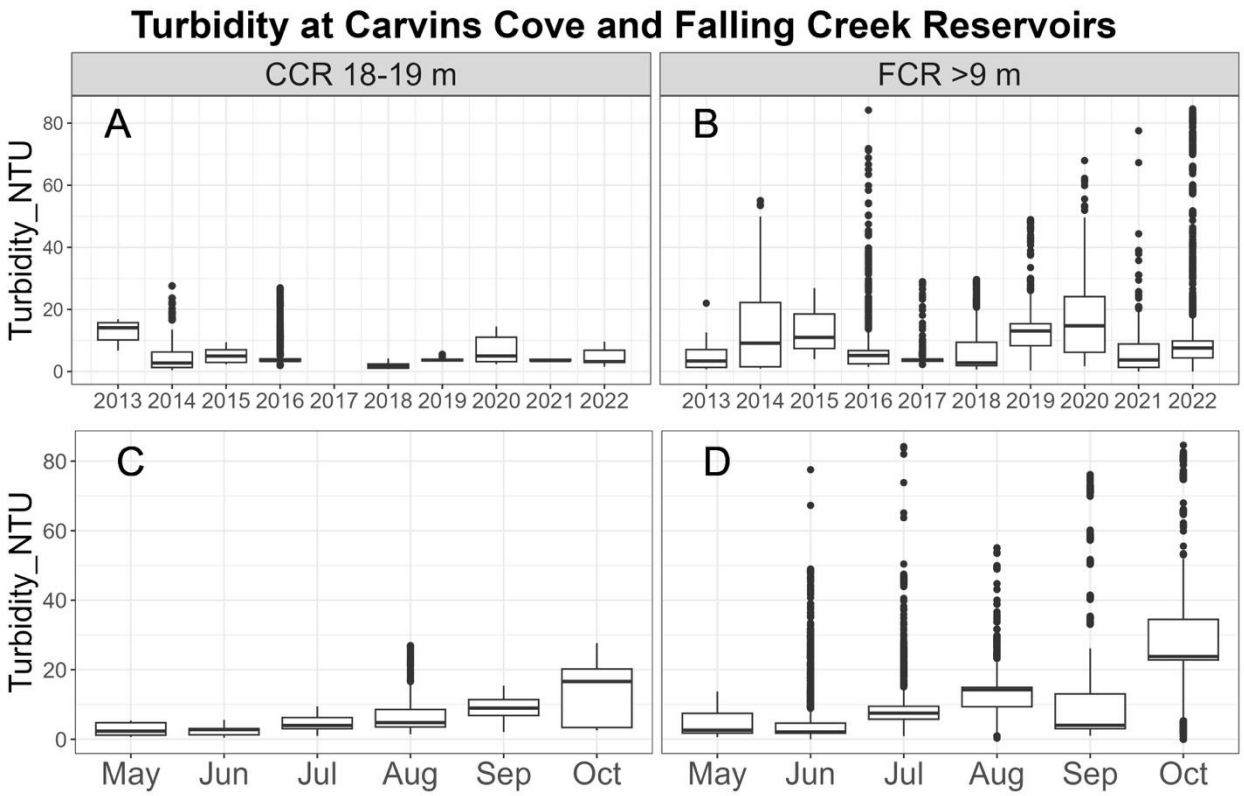

Figure S4: Boxplot of turbidity measurements from 2013-2022 in Carvins Cove Reservoir (CCR) and Falling Creek Reservoir (FCR) (Carey et al. 2024). A) Turbidity values from 18-19 m in CCR grouped by year of monitoring. B) Turbidity values from 9-10 m in FCR grouped by year of monitoring. The larger spread of data in FCR is at least partly due to greater number of CTD casts throughout the year in FCR and also due to the stirring up of sediment when the CTD hits the bottom. C) Turbidity values from 18-19 m in CCR aggregated by month of year during the stratified period. D) Turbidity values from >9 m in FCR grouped by month of year during the stratified period.

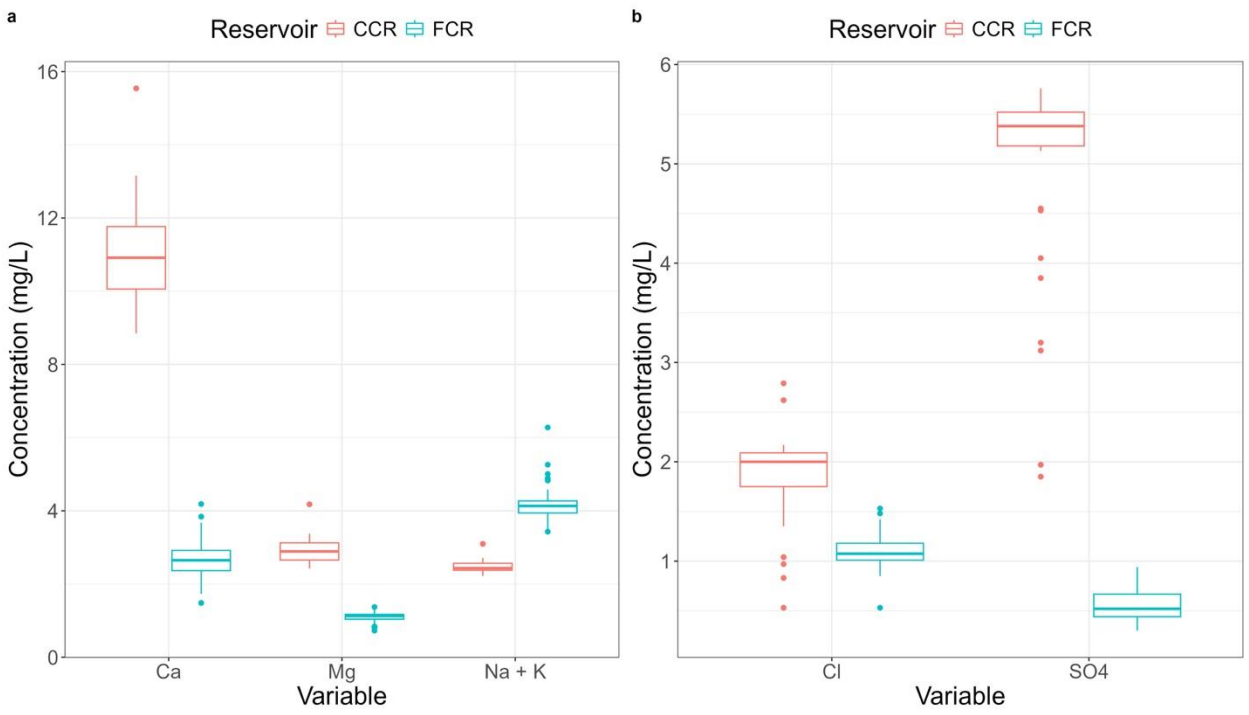

Figure S5. Major cation (a: Ca, Mg, Na + K; mg/L) and anion (b: Cl and SO_4; mg/L) concentrations in FCR and CCR in 2022. Samples collected from site 50. Although NO_3 was analyzed, concentrations in both reservoirs and tributaries were below the detection limit of 0.1 mg/L.

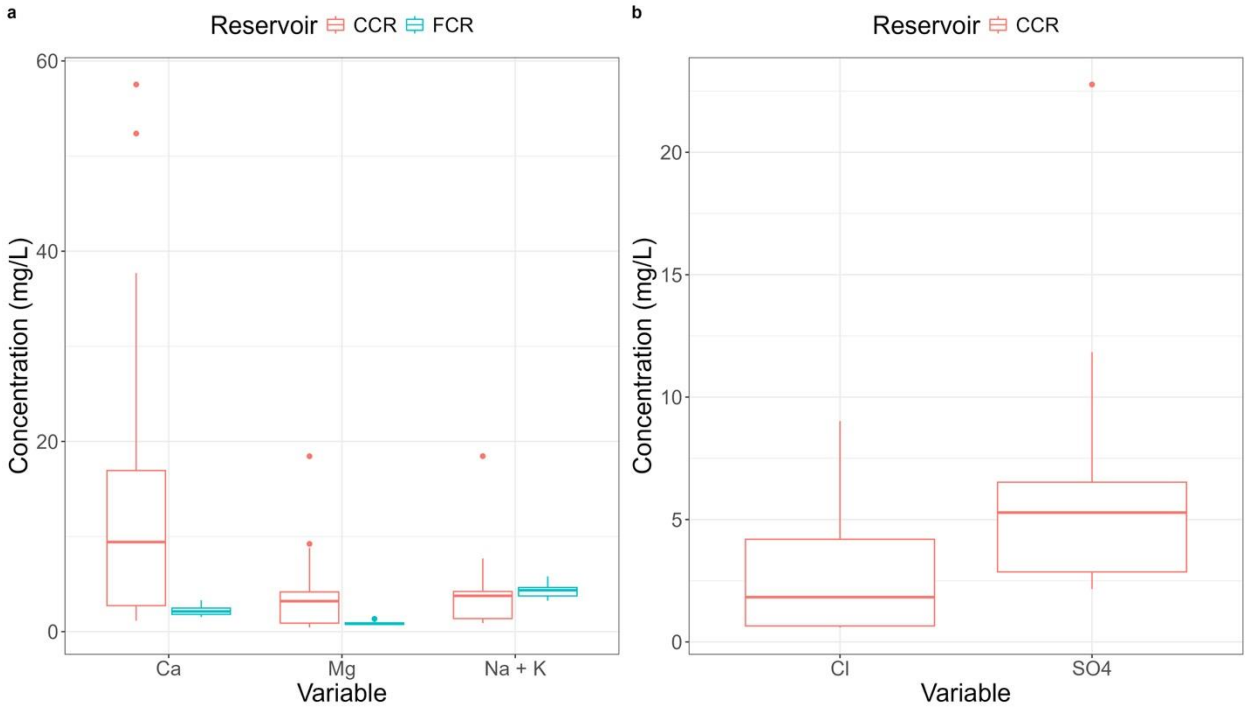

Figure S6. Major cation (a: Ca, Mg, Na + K; mg/L) and anion (b: Cl and SO_4; mg/L) concentrations in FCR and CCR tributaries in 2022. Although NO_3 was analyzed, concentrations were all below the detection limit of 0.1 mg/L. Note that anion samples were not collected for FCR tributaries.

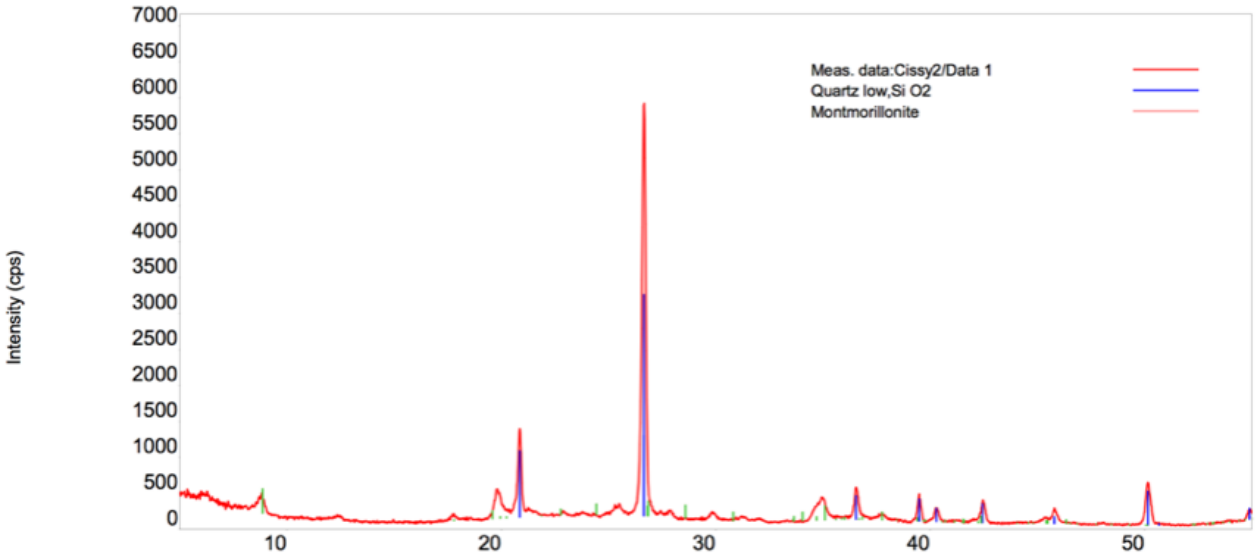

Figure S7: X-ray diffraction peaks detected in Carvins Cove Reservoir sediments collected from site 50 (red), with matches for montmorillonite (pink, a clay mineral) and quartz (blue) overlaid. Combined, quartz and clay minerals appear to comprise over 90% of minerals detected in the sediments.

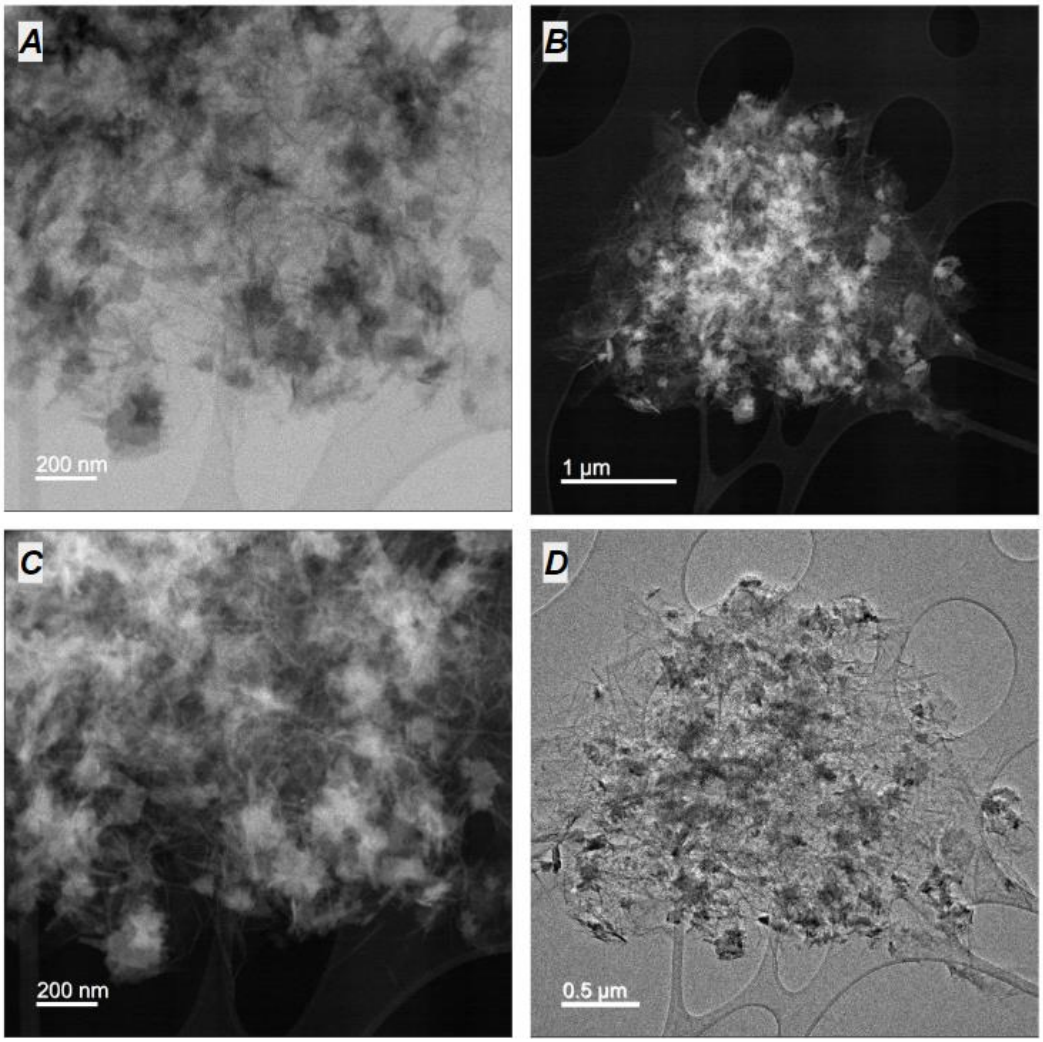

Figure S8. Transmission electron microscopy (TEM) images of a microscopic (<5 µm) particle suspended in the 24-hour pH 10 and 70 mg/L alkalinity solution at 12 hours. The particle is several µm in diameter and contains interlocking needle-like crystals of under 10 nm in diameter each. A) High magnification brightfield TEM image. B) Brightfield TEM image of the entire particle. C) Darkfield TEM image of the same view shown in A. D) Darkfield TEM image of the same view shown in B.

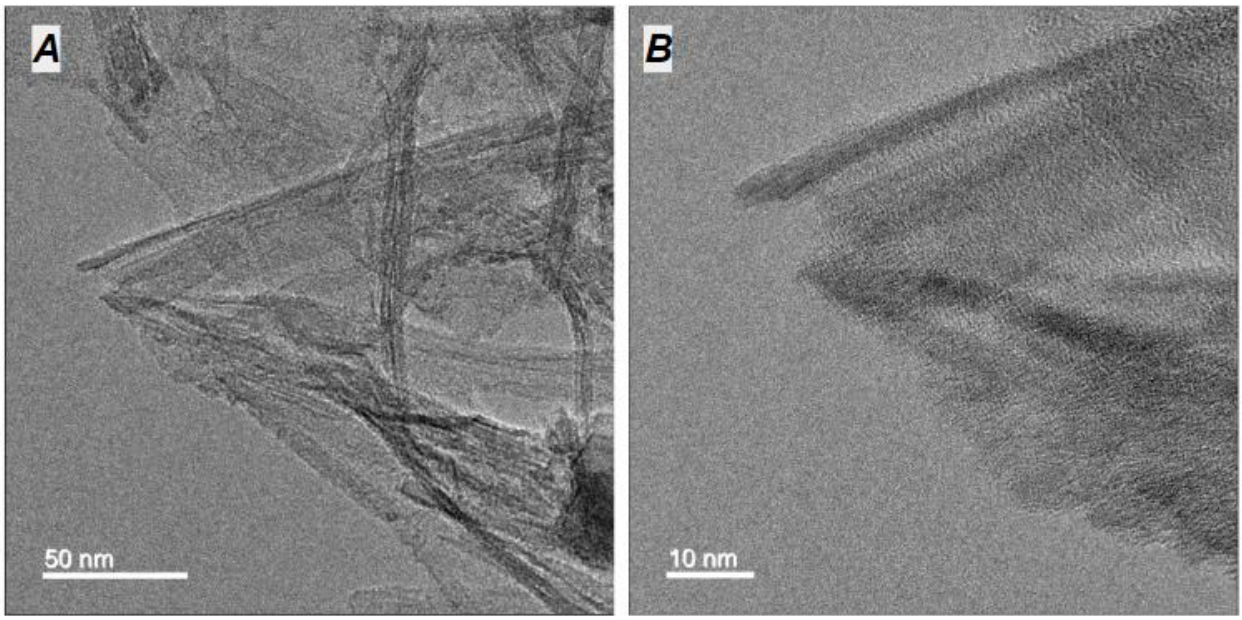

Figure S9. High magnification brightfield TEM images collected of the particle shown in Figure S8. A) Brightfield TEM image along the particle's periphery. B) Higher magnification brightfield TEM image in the same region shown in A. No crystal lattice fringes are visible.

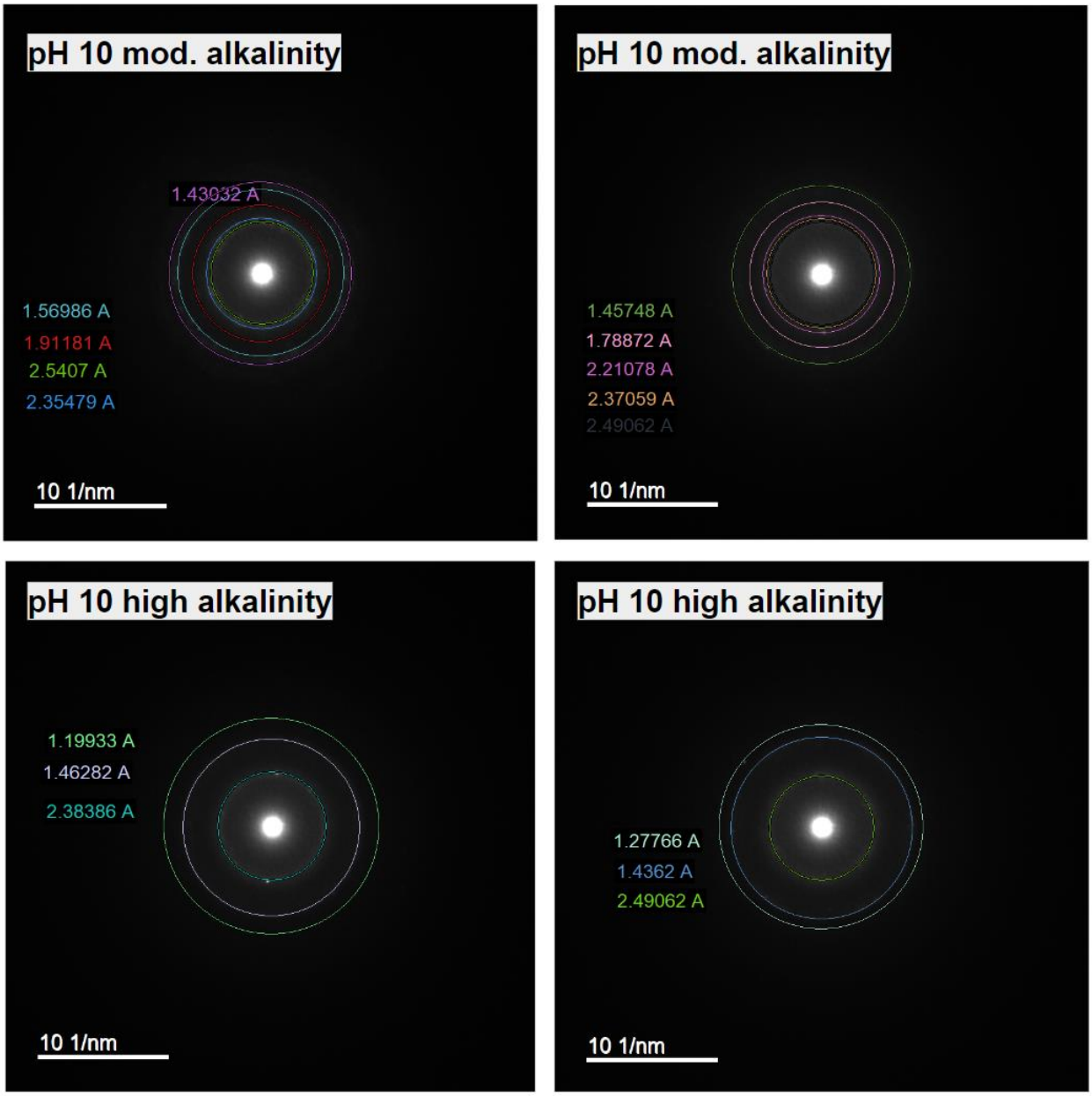

Figure S10. Diffraction rings obtained from selected area electron diffraction (SAED) of a particle collected from high pH (10) and moderate alkalinity (70 mg/L) solution (top) and high pH (10) and high alkalinity (250 mg/L) solution (bottom). Rings were manually identified and d-spacings were analyzed using the Gatan Digital Micrograph software package (Gatan Digital Micrograph, v. 3.5).